Operando optical tracking of single-particle ion dynamics in batteries

Alice J. Merryweather[1,2], Christoph Schnedermann[1]*, Quentin Jacquet[2], Clare P. Grey[2,]* & Akshay Rao[1,]*

[1] Cavendish Laboratory, University of Cambridge, J. J. Thomson Avenue, Cambridge CB3 0HE, United Kingdom

[2] Department of Chemistry, University of Cambridge, Lensfield Road, Cambridge CB2 1EW, United Kingdom

Key to advancing lithium-ion battery technology, in particular fast charging, is our ability to follow and understand the dynamic processes occurring in functioning materials under realistic conditions, in real time, and on the nano- to meso-scale. Currently, *operando* imaging of lithium-ion dynamics requires sophisticated synchrotron X-ray[1–7] or electron microscopy[8,9] techniques, which do not lend themselves to high-throughput material screening. This limits rapid and rational materials improvements. Here we introduce a simple laboratory-based, optical interferometric scattering microscope[10–13] to resolve nanoscopic lithium-ion dynamics in battery materials and apply it to follow cycling of the archetypical cathode material Li_xCoO_2.[14,15] We visualise the insulator-metal, solid solution and lithium ordering phase transitions directly and determine rates of lithium insertion and removal at the single-particle level, identifying different mechanisms on charge vs. discharge. Finally, we capture the dynamic formation of domain boundaries between different crystal orientations associated with the monoclinic lattice distortion at $Li_{0.5}CoO_2$.[16] The high throughput nature of our methodology allows many particles to be sampled across the entire electrode and, moving forward, will enable exploration of the role of dislocations, morphologies and cycling rate on battery degradation. The generality of our imaging concept means that it can be applied to study any battery electrode, and more broadly, systems where the transport of ions is associated with electronic or structural changes, including nanoionic films, ionic conducting polymers, photocatalytic materials and memristors.

Introduction

Lithium-ion batteries have emerged as the frontrunner technology for high-power, intermediate-scale energy storage, in a broad range of applications including electric vehicles

and portable devices. A major challenge associated with the development of improved batteries is to understand and optimise the processes by which lithium-ions intercalate into the active host materials. *Operando* characterisation techniques are needed to examine the fundamental limits to rate performance in working batteries.[17] However, tracking driven ionic motion in electrodes using established electrochemical methods is highly challenging, since the active particles are often intrinsically disordered at the particle and electrode level, and can behave heterogeneously.[1,18] Advanced *operando* synchrotron-based[1–7] and electron microscopy measurements[8,9] can probe the length and time scales required to examine individual particles, providing chemical and structural information. For example, *operando* transmission X-ray microscopy has revealed that non-uniform intercalation in Li_xFePO_4 causes compositional heterogeneity within particles to be enhanced during delithiation and supressed during lithiation.[2] However, such techniques are costly, time-intensive, can suffer from beam-induced sample degradation, and often require highly specialised cell geometries.[19]

While underused in battery research, optical microscopy techniques can overcome many of these disadvantages.[20–23] Here, we establish optical interferometric scattering microscopy (iSCAT)[10–13,24–26] as a rapid, low-cost imaging platform to visualise and quantify ion dynamics at the single-particle level. iSCAT, which uses elastic scattering of visible light to achieve fast acquisition times and high sensitivity, has not been applied to battery research until now. (Supplementary section 8 compares iSCAT with other *operando* imaging methods employed in battery research). We study Li_xCoO_2 (LCO, $0 < x < 1$), the archetypal layered cathode material which adopts the rhombohedral α–$NaFeO_2$ structure (Extended Data Figure 1a).[14,15] Despite being almost ubiquitous in portable electronics, the dynamics of phase transitions in LCO are not well understood: for instance, the reported lithium-ion diffusion coefficients vary over six orders of magnitude,[27–33] and the degree of compositional heterogeneity within single particles is little explored.[5,33]

Imaging lithium-ion transport in Li_xCoO_2

Operando iSCAT studies were carried out using an optically-accessible commercially-available half-cell (Figure 1a). The working electrode comprised single-crystal LCO particles (~10 μm average size, lengths comparable in all three dimensions, Extended Data Figure 1c,d), sparsely dispersed in a nanoparticulate carbon and polymer binder matrix, pressed onto an aluminium mesh current collector.

The galvanostatic performance of the electrode in the optical cell, at a rate of 2C, (Figure 1b,c) is in good agreement with previous reports[16] and with performance in a coin cell (Extended Data Figure 2). In this *n*C (C-rate) notation, *n* is the applied current divided by the theoretical current needed to (dis)charge the electrode material to its nominal theoretical (or more generally a specified) capacity in 1 hour. Prominent peaks in the differential capacity plots are resolved at ~4.0 V during delithiation and at ~3.8 V during lithiation (I and IV, Figure 1c), associated with a biphasic first-order transition from the semiconducting lithium-rich phase, of approximate composition $Li_{0.95}CoO_2$, to the metallic lithium-poor phase, of approximate composition $Li_{0.77}CoO_2$ (Supplementary section 5).[34,35] Smaller peaks in the differential capacity plots (II and III, Figure 1c) are associated with the lithium ordering transition at $Li_{0.5}CoO_2$ and the formation of a monoclinic phase.[16] The sloping regions between peaks I-II and III-IV correspond to a solid solution regime, during which the lithium content and cell parameters change continuously.

Full details of the iSCAT methodology can be found in the Methods section and Supplementary section 1. Briefly, as illustrated in Figure 1d,e, following widefield illumination at 780 nm ($\mathbf{E}_i$), the objective collects back-scattered light from the particle ($\mathbf{E}_s$), as well as reflected light from the glass window/electrolyte interface ($\mathbf{E}_r$). Both components are imaged onto a camera, where they interfere to produce the observed iSCAT image. The resulting iSCAT intensity is determined by the local dielectric properties of the sample material.[11,13,24–26] The method exploits the fundamental correlation between the local lithium content in LCO and local electronic structure (and thus the local dielectric properties),[36,37] which controls the scattering intensity. This allows the intercalation dynamics to be probed at the single-particle level, in real time with sub-5 nm precision (Supplementary section 3).[38,39] Critically, our approach works in the absence of optical absorption[40] and can be readily applied to examine multiple particles within the same electrode.

iSCAT images of several individual LCO particles were obtained during galvanostatic cycling. Raw iSCAT images (Figure 1f, Extended Data Figure 1e) show brightly scattering particles on top of a characteristic speckle pattern originating from scattering contributions from the surrounding carbon matrix. The relatively spatially-uniform intensity across each particle indicates a mostly-flat scattering surface, implying that the direction of observation is along the *c*-axis of the crystal structure, normal to the layers of CoO_6 octahedra (Extended Data Figure 1), and ideally suited to investigate the in-plane ion transport within the layered host lattice. For comparisons of iSCAT and scanning electron microscope (SEM) images, see Figure

1f and Extended Data Figure 1f-i. The imaging depth and effect of particle orientation is discussed further in Supplementary section 2.

iSCAT images were obtained during five electrochemical cycles at 2C for a representative LCO particle (~9.6 × 6.8 μm, Extended Data Figure 1e). As Figure 2a shows for one cycle (other cycles shown in Extended Data Figure 3), the iSCAT intensity increased by 1.6 times during delithiation (0 - 25 min), followed by an equivalent decrease upon lithiation (25 - 50 min), indicating good reversibility. This confirms that the changes in dielectric properties caused by the underlying electronic structural changes (Supplementary section 1)[34] are sufficient to allow the (de)lithiation processes to be monitored.

Next, we investigated the spatially-resolved ion dynamics during cycling (Figure 2b). The particle intensity remained relatively constant and homogenous at the beginning of the delithiation and during the sharp increase in cell potential to ~4.0 V (A). However, from 3 - 12 min, (exemplified by B, 10.2 min) the iSCAT images showed a substantial degree of spatial inhomogeneity in the form of bright and dark features. Similar inhomogeneous features were seen from 39 - 48 min, (exemplified by G, 43.8 min), corresponding to an equivalent state of charge upon lithiation. Examination of the full iSCAT video (Supplementary Video 1) revealed that these bright and dark features propagated across the visible surface of the particle. The durations of these moving features are aligned with the biphasic transitions identified in the overall electrochemistry (red shaded, Figure 2a), the moving features being assigned to propagating phase boundaries (discussed below). Short-lived propagating features were also observed at ~23 min and equivalently at ~27 min (blue shaded, Figure 2a), at times corresponding to the lithium ordering transitions (see below). Nearly spatially homogenous intensity changes occurred outside these transitions, *i.e.*, during the solid solution regimes (Figure 2b, C-F).

A further 15 particles across multiple electrodes were examined, yielding similar results, with an increase (decrease) in intensity upon delithiation (lithiation) and the observation of propagating phase boundaries, indicating that the described behaviour is general across the electrode(s). Detailed results for a second particle are presented later and included in Supplementary Videos 6-10.

The biphasic insulator-metal transition

The biphasic insulator-metal transition from the semiconducting $Li_{0.95}CoO_2$ to the metallic $Li_{0.77}CoO_2$ phase was then examined in more detail (red shaded, Figure 2a). Normalised sequential differential images, representing the fractional intensity change over 20

s, were extracted to visualise the phase boundaries (see Methods). During delithiation (Figure 3a), intensity changes initially occurred at the particle edges (4.3 min). After a ~3 min lag time, new features emerged and spread across the bulk of the particle, originating predominantly from the bottom edge of this particular particle, and developing into a ring-like structure (10.0 min). This ring feature progressively reduced in size and vanished at the end of the biphasic transition (11.0 – 11.7 min). The ring is assigned to the phase boundary between the lithium-rich phase in the middle and the newly formed lithium-poor phase growing inwards from the edges. This phase boundary movement is consistent with a so-called 'shrinking core' mechanism, where the new phase grows inwards from all active surfaces of the particle (Extended Data Figure 4a).[41,42] This behaviour was found in all cycles (Extended Data Figure 5). The velocity of the propagating phase boundaries was then extracted, yielding an average of ~20 nm s^{-1} (at 2C), reaching 37 nm s^{-1} at the end of the biphasic transition (Supplementary section 4).

Intriguingly, during lithiation (Figure 3b), a different behaviour was observed whereby a region of higher intensity first appeared in the top-right corner of the particle (39.3 min) and then spread across the whole particle (40.0 – 44.0 min). This process is best described as an 'intercalation wave' mechanism, where a single phase front (or small number of fronts) originating from one (or a small number of) nucleation point(s) moves across the particle (Extended Data Figure 4b).[41,43] While this mechanism occurred in all cycles, significant variations were found between cycles, both in the location of the first nucleation point and in the path taken by the new phase (Extended Data Figure 5).

Dynamic inhomogeneity between electrode particles can occur if the instantaneous current densities experienced by individual particles do not match the overall applied C-rate. For example, during the biphasic process found in $LiFePO_4$, only a small fraction of particles may be active at any given time,[7,44] leading to temporarily higher C-rates at the single-particle level. Thus, to investigate the LCO biphasic reaction further, the phase fractions in the particle were calculated and used to derive the effective C-rate for the particle under observation (see Methods). This single-particle 'biphasic C-rate' corresponds to the current required to achieve the observed pace of conversion between the two coexisting phases. Upon delithiation (Figure 3c), the biphasic reaction commenced at similar rate to that of the overall electrode (2C), with the new phase growing in from the particle edges and corners, to transform ~10% of the particle to the $Li_{0.77}CoO_2$ phase (4.3 min, Figure 3a). The single-particle C-rate then dropped, remaining low for ~3 min, before accelerating rapidly as the phase boundaries moved to form a shrinking ring, finally reaching ~9C at the end of the biphasic transition. This delithiation behaviour was

consistent across all cycles. Upon lithiation (Figure 3d), the new phase filled the particle at a C-rate oscillating around 2 – 5C for the selected cycle, but with significant variations between cycles, which are associated with the different paths travelled by the phase boundaries through the particle. (See Extended Data Figure 5 and Supplementary Videos 2-3 for sequential contrast images of the phase boundaries for all cycles).

A similar LCO particle from another electrode was monitored at applied C-rates from C/2 to 6C to explore the rate-dependant mechanisms. During delithiation at C/2, the integrated single-particle scattering intensity (Figure 4a) showed a peak during the biphasic transition (0-75 mA h g^{-1}) and a linear increase during the solid solution transition (75-155 mA h g^{-1}), with similar behaviour during the following lithiation. At all applied C-rates, the intensity changes during the solid solution reaction remained linear (with time) and reversible. However, as the current density was increased, the intensity peak at the biphasic transition shifted towards higher capacity during delithiation and lower capacity during lithiation, suggesting that the biphasic reaction in the observed particle lagged behind the ensemble electrochemistry. The single-particle C-rate (Figure 4b,c) increased sharply with increasing electrode current during the biphasic reaction, reaching 23C and 13C during delithiation and lithiation, respectively, at the highest cell current density (6C). The phase boundary progressed via an intercalation wave mechanism during lithiation at all applied C-rates (Figure 4d), while a shrinking core mechanism occurred during delithiation at 2 – 6C, consistent with the particle described above (Figure 3). At C/2 and 1C, however, delithiation appeared to follow a hybrid of the two mechanisms, with the new phase nucleating at two corners of the particle and propagating to finish at an edge - as opposed to the centre - of the particle (Supplementary Videos 6-10).

The shrinking core mechanism – seen here on delithiation – is a consequence of the higher lithium flux across the active electrochemical surface (for lithium-ion insertion/extraction, quantified via the charge transfer reaction rate), as compared to the lithium flux inside the particle (quantified via the lithium-ion diffusion rate) and is therefore the result of a 'diffusion-limited' process.[42,43] In contrast, the intercalation wave mechanism is 'charge transfer-limited' and results in the formation of a phase front, which can have different morphologies depending on the material/particle properties but features a reduced interfacial-area that propagates across the particle as the reaction proceeds.[43] That the shrinking core mechanism seen during high-rate delithiation appears to switch towards an intercalation wave mechanism at lower rates, is consistent with the decrease of the charge transfer rate at lower currents. This is consistent with recent simulations on LCO, and experimental work on large

graphite particles (>100 μm)[41,45]. However, the previous work makes no distinction between the mechanisms on delithiation and lithiation.

Phase field modelling[46] was performed to explore the origins of the observed differences between lithiation and delithiation and identify the parameters that control the phase boundary movement (Supplementary section 9). While highly simplified, our model explains the difference between the delithiation and lithiation mechanisms by considering the phase in which the charge transfer reaction occurs and the effect of the much lower lithium-ion diffusion coefficient in the lithium-rich vs. lithium-poor phases:[27,47] During rapid delithiation, once the lithium-poor phase has nucleated, the charge transfer reaction proceeds at both the lithium-rich and lithium-poor surfaces of the particle. Due to the sluggish lithium-ion transport in the lithium-rich phase, delithiation in this phase becomes diffusion-limited, and the lithium-poor phase builds up around all the active surfaces of the particle, resulting in a shrinking core mechanism (Supplementary Figure 8). On lithiation, although charge transfer (and thus lithiation) occurs in both phases initially, lithium builds up to saturation in the lithium-rich phase, shutting down this reaction pathway. Most of the charge transfer during lithiation proceeds instead via the high ionic mobility lithium-poor phase, leading to the intercalation wave mechanism for a large range of C-rates, as confirmed experimentally (Supplementary Figure 9).

The high single-particle C-rates of up to 23C observed at a 6C cell-level rate (Figure 4b-c), require very high lithium diffusion coefficients. To calculate a lower bound for the diffusion coefficient, delithiation of both particles during the biphasic process was simulated using various concentration-independent diffusion coefficients (Supplementary Figures 10-12). The extracted velocities of the phase boundaries were compared to the experimentally observed phase boundary velocities (Supplementary section 4). Good agreement was achieved using a chemical diffusion coefficient of ~10^{-9} cm^2 s^{-1} or higher, in line with the higher values estimated previously via theoretical[27] and muon spectroscopy[28] investigations (Supplementary Figure 13).

Lithium ordering at $Li_{0.5}CoO_2$

We now consider the lithium ordering transition (blue shaded, Figure 2a). Upon delithiation, the lithium ordering at $Li_{0.5}CoO_2$ removes the three-fold symmetry axis in the rhombohedral cell, leading to monoclinic symmetry. Early *operando* XRD studies reported a second-order transition,[16] but more recent synchrotron reports showed coexistence of the rhombohedral and monoclinic phases, suggesting a biphasic transition.[48] To explore this

transition, we computed the total normalised differential iSCAT images (*i.e.* the fractional intensity change for each pixel over the transition) for cycles 1 and 4 at 2C (other cycles in Extended Data Figure 6). In cycle 1 (Figure 5a), the particle intensity increased (decreased) relatively homogeneously upon ordering (disordering). By contrast, in cycle 4 (Figure 5b), the ordering transition produced bright sharp lines with three-fold symmetry in the particle, which disappeared again upon disordering. The absence of pronounced scattering lines in the bulk of the material in cycle 1 suggests that the monoclinic phase orientation was consistent across the whole particle (Figure 5c), *i.e.* only one monoclinic domain is present. By contrast, the appearance of bright lines with a three-fold symmetry in cycle 4 suggests the presence of three micron-sized ordered monoclinic domains, oriented at 120° with respect to each other, which can be distinguished by brightly scattering domain boundaries (Figure 5d).

To follow the dynamic evolution of these structures, normalised sequential differential images (5 s frame interval) for the transition during lithiation were then analysed (Supplementary Videos 4-5, including delithiation). In cycle 1 (Figure 5e), two phase fronts are identified which emerge from opposite sides of the particle and approach each other head-on, travelling at a velocity of ~70 nm s^{-1}. By comparison, in cycle 4 (Figure 5f), the disordered phases grow in from three different locations separated by the visible domain boundaries. It should be noted that the phase boundaries move significantly faster than for the insulator-metal biphasic transition, largely because they involve long-range ordering of lithium-ions, rather than a (significant) change in lithium-ion concentration.[16] The rapid image acquisition capabilities of optical microscopy are advantageous in studying such fast phase transitions.

Our work builds on the previous *ex-situ* electron diffraction observation of several ordered domains with three distinct orientations of the monoclinic phase within a single particle,[49] by observing the dynamics of the domain formation in real time. Furthermore, we show for this phase transition involving symmetry breaking, when new phases originate from multiple nucleation points, they cannot readily fuse together if their orientations differ. The particle retains some memory of the nucleation conditions in the form of domains. This is opposed to the case of the insulator-metal biphasic transition discussed above, for which symmetry is conserved across the phase transition, so that separate regions of the new phase can join together seamlessly. Considering the excellent cycling stability of LCO between 3.0 V and 4.2 V, the presence of the monoclinic domains at $Li_{0.5}CoO_2$ does not appear to be detrimental, probably because the monoclinic distortion leads to only a small deformation of the unit cell.[16] This is not the case for the high voltage O3-O1 transition that occurs at a

composition of approximately $Li_{0.15}CoO_2$, during which there are much larger changes to the cell parameters.[15]

Conclusions

In conclusion, we have established iSCAT microscopy as a powerful tool to track and quantify phase transitions in LCO on the nanoscale, in real time and under realistic operating conditions. The solid solution, biphasic and lithium ordering transitions were clearly resolved and correlated to the ensemble electrochemistry. Mechanistically, we identified a preference for a shrinking core mechanism for delithiation and an intercalation wave mechanism for lithiation during the biphasic transition. These observations were rationalised in terms of the differences in lithium diffusivity in the two phases, with support from phase field modelling. Single-particle C-rates and phase boundary velocities were extracted to show that individual particles are capable of sustaining much higher C-rates than the overall C-rate of the electrode, highlighting the inherent high-rate capabilities of LCO. Additionally, we observed the real-time formation and destruction of domains in monoclinic $Li_{0.5}CoO_2$.

The results presented here highlight the ability of this scattering microscopy methodology to provide real-time insights into nanoscale electronic or structural phase transitions. Due to its straightforward lab-based implementation, we hope that iSCAT will become an indispensable tool for high-throughput material discovery and mechanistic studies (Supplementary section 7), to complement existing synchrotron-based methodologies. For example, future work could examine the effects of grain boundaries and crystal defects[6] on phase transitions and ion intercalation mechanisms. Critically, the principle of using light-scattering to probe charge transport[23,50,51] and electronic structure changes is broadly applicable to a wide range of materials (Supplementary section 6) and promises to be generally valuable for the study of ferroelectrics, nanoionics, bioelectronics, photocatalytic materials, and memristors, in addition to batteries.

References

1. Yu, Y.-S. *et al.* Three-dimensional localization of nanoscale battery reactions using soft X-ray tomography. *Nat. Commun.* **9**, 921 (2018).
2. Lim, J. *et al.* Origin and hysteresis of lithium compositional spatiodynamics within battery primary particles. *Science* **353**, 566–571 (2016).
3. Li, S. *et al.* Mutual modulation between surface chemistry and bulk microstructure within secondary particles of nickel-rich layered oxides. *Nat. Commun.* **11**, 4433 (2020).
4. Tsai, P.-C. *et al.* Single-particle measurements of electrochemical kinetics in NMC and NCA cathodes for Li-ion batteries. *Energy Environ. Sci.* **11**, 860–871 (2018).
5. Xu, Y. *et al.* In situ visualization of state-of-charge heterogeneity within a $LiCoO_2$ particle that evolves upon cycling at different rates. *ACS Energy Lett.* **2**, 1240–1245 (2017).
6. Singer, A. *et al.* Nucleation of dislocations and their dynamics in layered oxide cathode materials during battery charging. *Nat. Energy* **3**, 641–647 (2018).
7. Zhang, X. *et al.* Direct view on the phase evolution in individual $LiFePO_4$ nanoparticles during Li-ion battery cycling. *Nat. Commun.* **6**, 8333 (2015).
8. Holtz, M. E. *et al.* Nanoscale imaging of lithium ion distribution during in situ operation of battery electrode and electrolyte. *Nano Lett.* **14**, 1453–1459 (2014).
9. He, K. *et al.* Operando liquid cell electron microscopy of discharge and charge kinetics in lithium-oxygen batteries. *Nano Energy* **49**, 338–345 (2018).
10. Lindfors, K., Kalkbrenner, T., Stoller, P. & Sandoghdar, V. Detection and spectroscopy of gold nanoparticles using supercontinuum white light confocal microscopy. *Phys. Rev. Lett.* **93**, 037401 (2004).
11. Ortega-Arroyo, J. & Kukura, P. Interferometric scattering microscopy (iSCAT): new frontiers in ultrafast and ultrasensitive optical microscopy. *Phys. Chem. Chem. Phys.* **14**, 15625–15636 (2012).
12. Young, G. & Kukura, P. Interferometric Scattering Microscopy. *Annu. Rev. Phys. Chem.* **70**, 301-322 (2019).

13. Taylor, R.W. & Sandoghdar V. Interferometric scattering (iSCAT) microscopy and related techniques. In: Astratov V. (ed) *Label-Free Super-Resolution Microscopy*. Springer, Cham. (2019)

14. Mizushima, K., Jones, P. C., Wiseman, P. J. & Goodenough, J. B. Li_xCoO_2 ($0 < x \leq$ l): A new cathode material for batteries of high energy density. *Mater. Res. Bull.* **15**, 783–789 (1980).

15. Amatucci, G. G., Tarascon, J. M. & Klein, L. C. CoO_2, the end member of the Li_xCoO_2 solid solution. *J. Electrochem. Soc.* **143**, 1114 (1996).

16. Reimers, J. N. & Dahn, J. R. Electrochemical and in situ X-ray diffraction studies of lithium intercalation in Li_xCoO_2. *J. Electrochem. Soc.* **139**, 2091–2097 (1992).

17. Liu, H. *et al.* Capturing metastable structures during high-rate cycling of $LiFePO_4$ nanoparticle electrodes. *Science* **344**, 1252817 (2014).

18. Zhang, Y., Yang, Z. & Tian, C. Probing and quantifying cathode charge heterogeneity in Li ion batteries. *J. Mater. Chem. A* **7**, 23628–23661 (2019).

19. Wu, Y. & Liu, N. Visualizing battery reactions and processes by using in situ and in operando microscopies. *Chem* **4**, 438–465 (2018).

20. Otoyama, M., Kowada, H., Sakuda, A., Tatsumisago, M. & Hayashi, A. Operando confocal microscopy for dynamic changes of Li^+ ion conduction path in graphite electrode layers of all-solid-state batteries. *J. Phys. Chem. Lett.* **11**, 900–904 (2020).

21. Kazyak, E. *et al.* Li penetration in ceramic solid electrolytes: operando microscopy analysis of morphology, propagation, and reversibility. *Matter* **2**, 1025–1048 (2020).

22. Wood, K. N. *et al.* Dendrites and pits: untangling the complex behavior of lithium metal anodes through operando video microscopy. *ACS Cent. Sci.* **2**, 790–801 (2016).

23. Namink, K., Meng, X., Koper, M. T. M., Kukura, P. & Faez, S. Electric-double-layer-modulation microscopy. *Phys. Rev. Applied* **13**, 044065 (2020).

24. Ortega Arroyo, J., Cole, D. & Kukura, P. Interferometric scattering microscopy and its combination with single-molecule fluorescence imaging. *Nat. Protoc.* **11**, 617–633 (2016).

25. Piliarik, M. & Sandoghdar, V. Direct optical sensing of single unlabelled proteins and super-resolution imaging of their binding sites. *Nat. Commun.* **5**, 4495 (2014).

26. Mahmoodabadi, R. G. *et al.* Point spread function in interferometric scattering microscopy (iSCAT). Part I: aberrations in defocusing and axial localization. *Opt. Express* **28**, 25969–25988 (2020).

27. Van der Ven, A. & Ceder, G. Lithium diffusion in layered Li_xCoO_2. *Electrochem. Solid-State Lett.* **3**, 301 (2000).

28. Sugiyama, J. *et al.* Li diffusion in Li_xCoO_2 probed by muon-spin spectroscopy. *Phys. Rev. Lett.* **103**, 147601 (2009).

29. Jang, Y.-I., Neudecker, B. J. & Dudney, N. J. Lithium diffusion in Li_xCoO_2 ($0.45 < x < 0.7$) intercalation cathodes. *Electrochem. Solid-State Lett.* **4**, A74 (2001).

30. Xia, H., Lu, L. & Ceder, G. Li diffusion in $LiCoO_2$ thin films prepared by pulsed laser deposition. *J. Power Sources* **159**, 1422–1427 (2006).

31. Xie, J. *et al.* Orientation dependence of Li–ion diffusion kinetics in $LiCoO_2$ thin films prepared by RF magnetron sputtering. *Solid State Ion.* **179**, 362–370 (2008).

32. Takeuchi, S. *et al.* Epitaxial $LiCoO_2$ films as a model system for fundamental electrochemical studies of positive electrodes. *ACS Appl. Mater. Interfaces* **7**, 7901–7911 (2015).

33. Dokko, K. *et al.* Kinetic characterization of single particles of $LiCoO_2$ by AC impedance and potential step methods. *J. Electrochem. Soc.* **148**, A422 (2001).

34. Ménétrier, M., Saadoune, I., Levasseur, S. & Delmas, C. The insulator-metal transition upon lithium deintercalation from $LiCoO_2$: electronic properties and ^{7}Li NMR study. *J. Mater. Chem.* **9**, 1135–1140 (1999).

35. Ménétrier, M., Carlier, D., Blangero, M. & Delmas, C. On "really" stoichiometric $LiCoO_2$. *Electrochem. Solid-State Lett.* **11**, A179 (2008).

36. Liu, H. L. *et al.* Electronic structure and lattice dynamics of Li_xCoO_2 single crystals. *New J. Phys.* **17**, 103004 (2015).

37. Rubin, M., von Rottkay, K., Wen, S.-J., Özer, N. & Slack, J. Optical indices of lithiated electrochromic oxides. *Sol. Energy Mater. Sol. Cells* **54**, 49–57 (1998).

38. Sung, J. *et al.* Long-range ballistic propagation of carriers in methylammonium lead iodide perovskite thin films. *Nat. Phys.* **16**, 171–176 (2020).

39. Schnedermann *et al*. Ultrafast tracking of exciton and charge carrier transport in optoelectronic materials on the nanometer scale, *J. Phys. Chem. Lett*. **10**, 6727–6733 (2019).

40. Evans, R. C., Nilsson, Z. N. & Sambur, J. B. High-throughput single-nanoparticle-level imaging of electrochemical ion insertion reactions. *Anal. Chem.* **91**, 14983–14991 (2019).

41. Fraggedakis, D. *et al.* A scaling law to determine phase morphologies during ion intercalation. *Energy Environ. Sci.* **13**, 2142–2152 (2020).

42. Zhang, W., Srinivasan, S. & Ploehn, H. J. Analysis of transient hydrogen uptake by metal alloy particles. *J. Electrochem. Soc.* **143**, 4039 (1996).

43. Singh, G. K., Ceder, G. & Bazant, M. Z. Intercalation dynamics in rechargeable battery materials: general theory and phase-transformation waves in $LiFePO_4$. *Electrochim. Acta* **53**, 7599–7613 (2008).

44. Li, Y. *et al.* Current-induced transition from particle-by-particle to concurrent intercalation in phase-separating battery electrodes. *Nat. Mater.* **13**, 1149–1156 (2014).

45. Nadkarni, N., Zhou, T., Fraggedakis, D., Gao, T. & Bazant, M. Z. Modeling the metal–insulator phase transition in Li_xCoO_2 for energy and information storage. *Adv. Funct. Mater.* **29**, 1902821 (2019).

46. Bazant, M. Z. Theory of chemical kinetics and charge transfer based on nonequilibrium thermodynamics. *Acc. Chem. Res.* **46**, 1144–1160 (2013).

47. Van der Ven, A., Bhattacharya, J. & Belak, A. A. Understanding Li diffusion in Li-intercalation compounds. *Acc. Chem. Res.* **46**, 1216–1225 (2013).

48. Morcrette, M. *et al.* In situ X-ray diffraction techniques as a powerful tool to study battery electrode materials. *Electrochim. Acta* **47**, 3137–3149 (2002).

49. Shao-Horn, Y., Levasseur, S., Weill, F. & Delmas, C. Probing lithium and vacancy ordering in O3 Layered Li_xCoO_2 ($x \sim 0.5$). *J. Electrochem. Soc.* **150**, 9 (2003).

50. Delor, M., Weaver, H. L., Yu, Q. & Ginsberg, N. S. Imaging material functionality through three-dimensional nanoscale tracking of energy flow. *Nat. Mater.* **19**, 56–62 (2020).

51. Folie, B. D. *et al.* Effect of anisotropic confinement on electronic structure and dynamics of band edge excitons in inorganic perovskite nanowires. *J. Phys. Chem. A* **124**, 1867–1876 (2020).

52. Chen, K.-H. *et al.* Dead lithium: mass transport effects on voltage, capacity, and failure of lithium metal anodes. *J. Mater. Chem. A* **5**, 11671–11681 (2017).

Figures

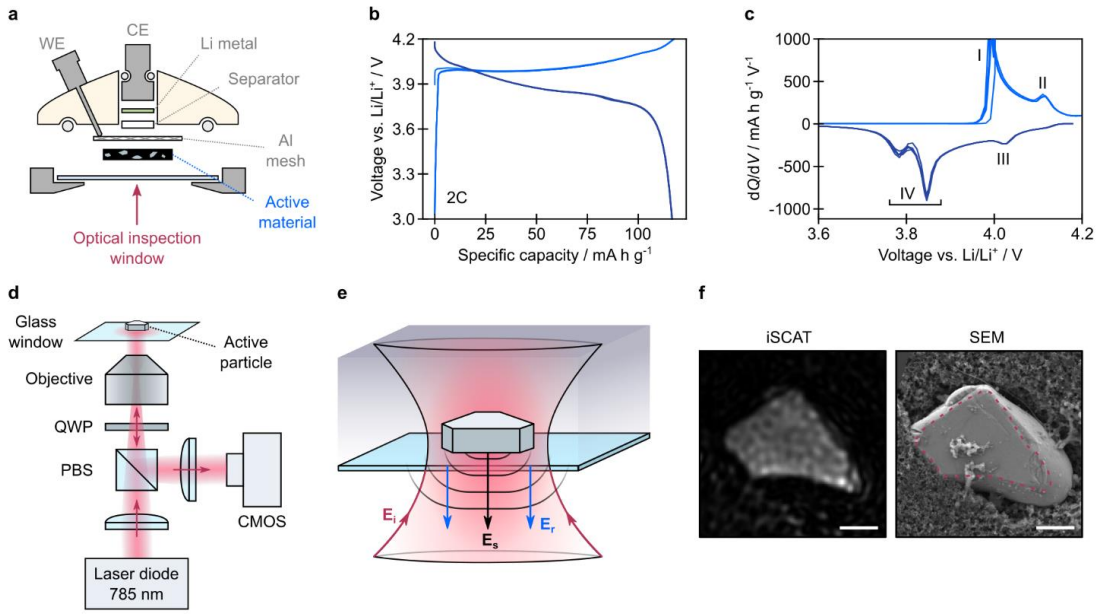

Figure 1: Electrochemical performance and interferometric scattering microscopy of a LCO electrode.

a Geometry of the optical microscopy half-cell. (WE = working electrode, CE = counter electrode). The counter electrode was lithium metal, the separator was glass fibre, and the cell stack was wet with standard carbonate liquid electrolyte (LP30). **b** Galvanostatic cycling (2C, 5 cycles) of the LCO electrode during *operando* optical measurements. **c** Corresponding differential capacity (d*Q*/d*V*) plots. The peaks attributed to biphasic transitions (I and IV) and lithium ordering (II and III) are indicated. The splitting of IV into two distinct peaks on discharging is ascribed to an anode process, the Li stripping mechanism switching from a process involving dissolution from mossy Li dendrites to pitting and dissolution of bulk Li.[52] **d** Optical setup of the interferometric scattering (iSCAT) microscope. (PBS = polarising beam splitter, QWP = quarter-wave plate, CMOS = complementary metal oxide semiconductor camera). **e** Schematic diagram of iSCAT signal generation. Incident light ($\mathbf{E}_i$) is focussed onto an active particle of interest in the working electrode. The collected light includes a contribution scattered from the surface of the active particle ($\mathbf{E}_s$) and a reference contribution reflected from the top interface of the glass window ($\mathbf{E}_r$). **f** Left: iSCAT image of a single active LCO particle in the electrode. Intensity values are normalised to a linear scale between 0 (black) and 1 (white). Right: Corresponding scanning electron microscopy (SEM) image of the same LCO particle. The red dashed line represents the outline of the bright region in the iSCAT image. Both scale bars are 2 µm.

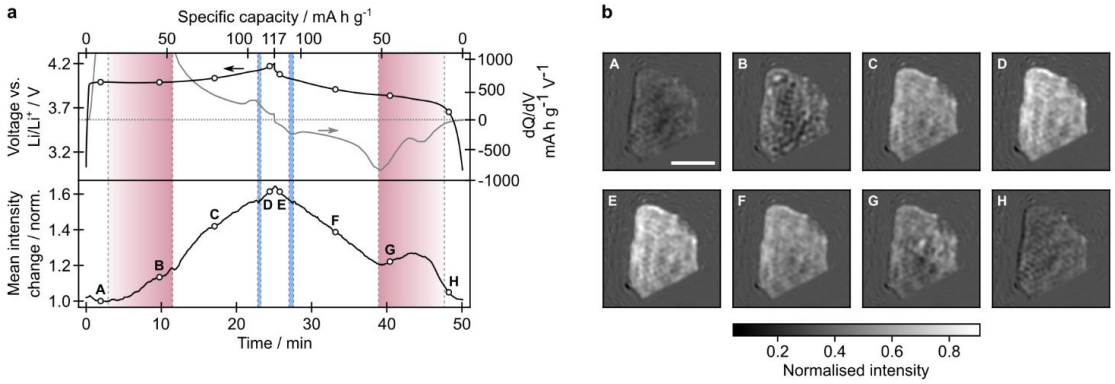

Figure 2: Overview of the optical response of an active particle during battery operation.
a Top: Galvanostatic and differential capacity plots shown in black and grey respectively, as a function of time (cycle 4, as plotted in Figure 1b,c). Bottom: iSCAT intensity change averaged over the active particle shown in Extended Data Figure 1e, during galvanostatic cycling. Vertical red and blue shaded regions correspond to the durations of the biphasic and lithium ordering transitions, respectively, identified from images of this particle. **b** Background-subtracted iSCAT images of the active particle at the time-points indicated in panel a. Background subtraction was achieved by subtracting reference values for each pixel at the beginning of the cycle from the corresponding pixels in all subsequent images. Scale bar is 5 μm.

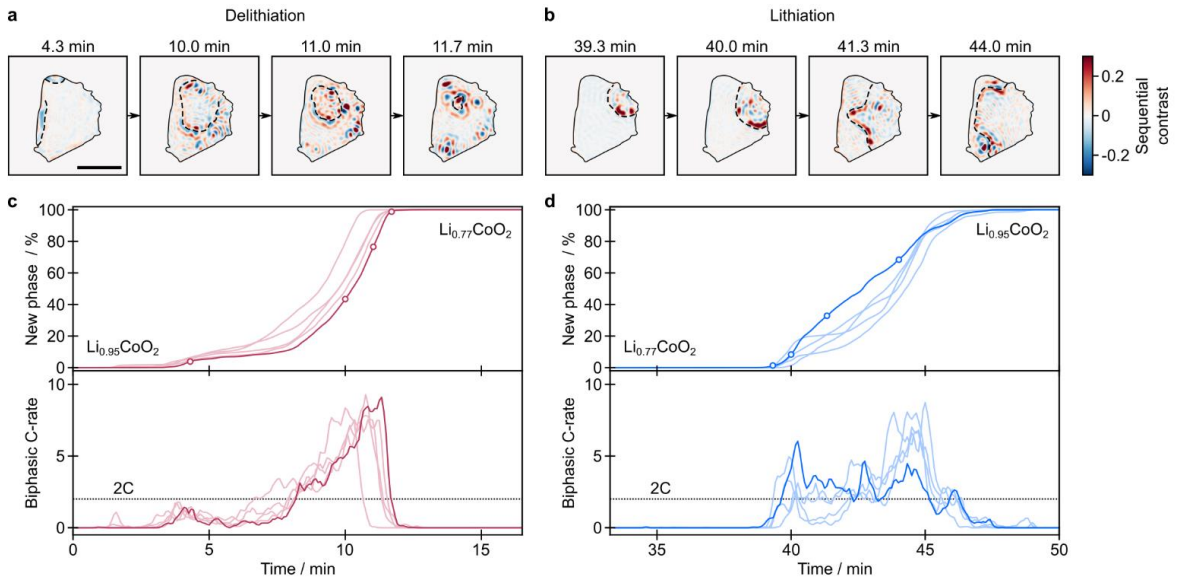

Figure 3: Behaviour of biphasic phase transitions upon delithiation and lithiation.
a, b Sequential differential images of the active particle (shown in Extended Data Figure 1e) upon delithiation and lithiation, respectively, during the biphasic transition (in cycle 4). The black dashed lines are a guide for the eye, representing the phase boundary position. Sequential contrast is obtained by dividing pixel intensity values by those from 20 s earlier, then subtracting 1, to represent the intensity changes over this timescale. Scale bar is 5 μm. **c, d** Top: Phase fraction of $Li_{0.77}CoO_2$ (delithiation) and $Li_{0.95}CoO_2$ (lithiation), respectively, as a function of time. All 5 cycles are shown, and time is measured from the start of each cycle. Time-points corresponding to the images in **a** and **b** are indicated as open circles on the traces for cycle 4 (darker shade). Bottom: The instantaneous single-particle C-rate for the biphasic transition, as obtained from the change in phase fraction.

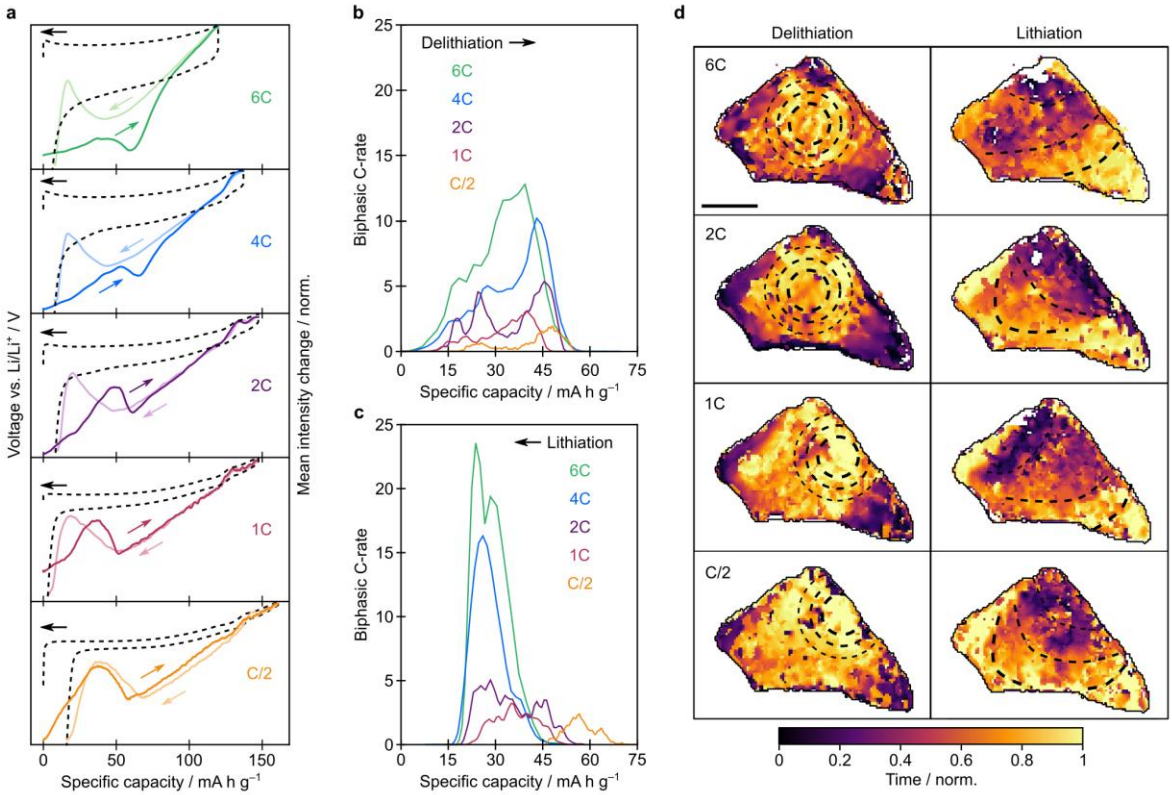

Figure 4: Behaviour of biphasic phase transitions at various applied current densities.
a Galvanostatic cell capacity plots with a voltage window of 3.0 V to 4.3 V (black dashed) for applied C-rates ranging from C/2 to 6C, with iSCAT intensity averaged over a single active particle during delithiation (dark colour) and lithiation (light colour). Note that the apparent loss of coulombic efficiency at slower cycling rates is the result of parasitic side reactions, while the LCO electrochemistry remains reversible. **b, c** Instantaneous single-particle C-rates for the biphasic transition during delithiation and lithiation, respectively. **d** Progression of the phase boundary through the active particle during the biphasic transition, for delithiation and lithiation. The colour scale represents the time at which each pixel experienced the phase boundary, as a fraction of the total duration of the biphasic transition. Solid black lines clarify the observed outline of the particle. Black dashed circles and lines are a guide to the eye to visualise the progression of the phase boundary. Scale bar is 2 μm.

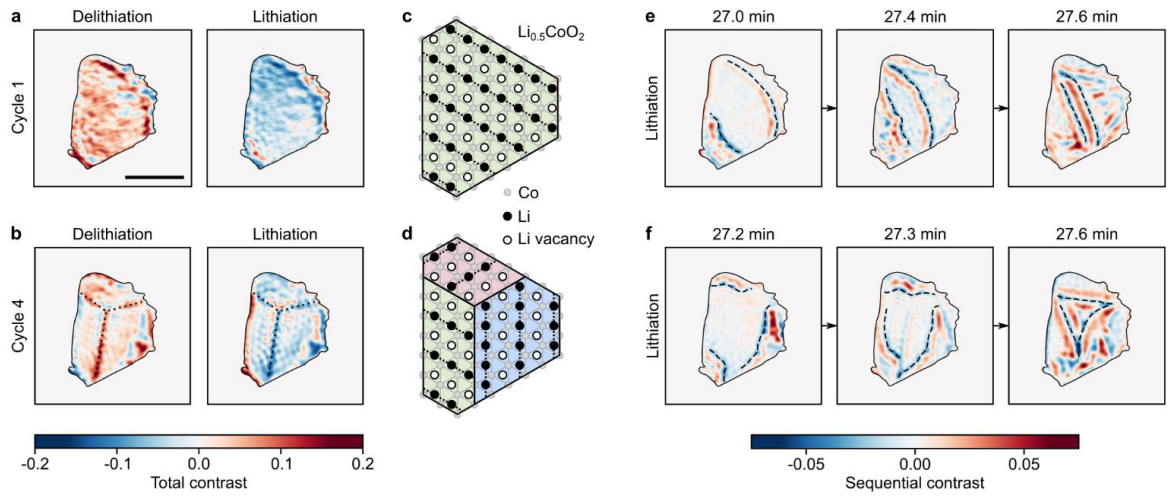

Figure 5: Dynamics of the monoclinic distortion at $Li_{0.5}CoO_2$, with and without domain formation. **a, b** Images showing the total contrast resulting from lithium ordering in cycle 1 and cycle 4, respectively, for delithiation and lithiation. These were obtained by dividing pixel intensity values immediately after the transition by those from immediately before the transition, then subtracting 1, to represent the total intensity change caused by the transition. Scale bar is 5 μm. For cycle 4, the formation of the ordered state produces domain-like features, with three regions separated by bright lines at approximately 120°. **c, d** Schematics of a particle of $Li_{0.5}CoO_2$ with lithium-ions ordered into rows. The cases for a single monoclinic domain and for three monoclinic domains (with orientations of the rows differing by 120°) are shown, respectively. **e, f** Differential images for cycle 1 and cycle 4, respectively, during the transition causing lithium disordering upon lithiation. Sequential contrast is obtained by dividing pixel intensity values by those from 5 s earlier, then subtracting 1, to represent the intensity changes over this timescale.

Methods

1. Sample preparation

Self-standing electrode films were prepared from LCO powder (Sigma-Aldrich), Super P™ carbon and polytetrafluoroethylene suspension (PTFE, 60% in water), combined by grinding together with ethanol in a pestle and mortar. The dry mass ratios of LCO, carbon and PTFE were 20%, 46% and 34%, respectively. Upon drying to a workable consistency, the mixture was rolled flat into a porous self-standing film with a thickness of ~150 μm. The film was fully dried (vacuum oven, 100°C, overnight) before cutting electrode disks of 5 mm diameter. The electrodes were stored in a dry argon atmosphere prior to use.

The optical cell (Figure 1a) is based on a commercially available model (EL-CELL, ECC-Opto-Std test cell), with a homemade lid that was designed to be compatible with our microscope objective (100×, UPLSAPO100XO, Olympus) and glass observation windows. The cell was assembled in a dry argon atmosphere. The working electrode consisted of the self-standing film, pressed atop an aluminium mesh current collector. The counter electrode was lithium metal, the separator was glass fibre (Whatman, GF/B glass microfiber filter), and the cell stack was wet with LP30 liquid electrolyte (Sigma-Alrich, 1 M $LiPF_6$ in a 50:50 mixture of ethylene carbonate and dimethyl carbonate). Following assembly, the cell was galvanostatically cycled ~20 times at 2C prior to obtaining iSCAT measurements. Throughout this work, the quoted C-rates are based on a practical specific capacity of 140 mA h g^{-1}.

2. Optical setup

The interferometric scattering microscopy (iSCAT) setup used in this work is adapted from previous work by Ortega Arroyo and Kukura.[24] In our implementation, the light source is a high-stability pulsed laser diode (LDHP-C-780, SEPIA II laser driver, PicoQuant), which generates ~60 ps pulses at a central wavelength of 780 nm with a maximum repetition rate of 80 MHz. A near-IR coated telecentric lens system with a 40 μm pinhole (Thorlabs) at the focus selects a Gaussian spatial mode and magnifies the beam to a diameter of ~1 cm. This beam is directed into a home-built inverted widefield microscope equipped with a 1.4 NA oil immersion objective (100×, UPLSAPO100XO, Olympus) and a custom-made 3D nano-positioned sample stage (Attocube, ECSx3030/AL/RT/NUM).

The illumination path of the microscope consists of a near-IR coated widefield lens (F = 500 mm, AC254-500B, Thorlabs) placed one focal length away from the back-focal plane of the objective. This results in a widefield Gaussian illumination profile with a full width at half-

maximum (FWHM) of ~20 μm in the objective focus. Before reaching the objective, the beam is transmitted through a linearly polarising beam splitter cube (PBS252, Thorlabs) and a quarter waveplate (QWP, AHWP05M-600, Thorlabs) to illuminate the sample with circularly polarised light. In this work, circularly polarised illumination was selected in an effort to avoid dipolar selectivity. We note that linearly polarised light may produce additional insights, as it could probe sample anisotropy that may arise if dipoles become ordered in certain orientations.

After interaction with the sample, the reflected/scattered light contributions are collected by the illumination objective and directed back through the QWP. After passing through the QWP for the second time, the returning light has acquired a 90° polarisation shift compared to the illumination beam, which results in the returning light being reflected from the polarising beam splitter cube. The QWP was rotated to maximise the collection efficiency for the reflected light. A near-IR coated tube lens (F=500 mm, AC254-500B, Thorlabs) placed one focal length away from the objective's back-focal plane finally images the returning light onto a 12-bit CMOS camera (FLIR, Grashopper3, GS3-U3-23S6M-C). The overall magnification of this imaging system is 278× (21.1 nm/px), and was confirmed with a resolution target. The 780 nm illumination wavelength and NA of 1.4 produce a lateral resolution of ~280 nm (FWHM).

For the C-rate-dependence studies carried out in Figure 4 (and the iSCAT images in Figure 1f, Extended Data Figure 1f-i), we instead imaged the returning light onto a 16-bit sCMOS camera (Hamamatsu, ORCA Flash 4 V3). Here, light collected by the objective was sent through a conjugated telescope to reduce the beam by a factor of 1.25 (F = 500 mm and F = 400 mm, AC254-B, Thorlabs), before being imaged via a final tube lens (F = 500 mm, AC254-500B, Thorlabs) onto the camera. The overall magnification was 222× (29.3 nm/px).

Actively stabilised focus control was implemented to avoid long-term focus drift and electrochemically-induced defocussing. To achieve this, we used a reflection-based variation of a previously described line-autofocus procedure that operates based on total internal reflection of a reference beam.[24] An approach based on total internal reflection is not feasible for most battery systems due to the high refractive index electrolyte. The reference beam was generated by a 980 nm diode laser (CPS980S, Thorlabs) and focussed via a dichroic mirror (DMSP900, Thorlabs) onto the back-focal plane of the objective. The reflected beam was picked off after the objective, focused through a non-conjugated cylindrical lens (F = 200 mm, Thorlabs) into a line and detected by a CMOS camera (DCC1545M, Thorlabs). The refresh rate for the focus control was set to 10 Hz and allowed us to achieve a steady focus position with a standard deviation of 13 nm over the full course of the experiment.

3. Data Acquisition

For the experiment presented in Figures 2, 3, and 5, images were acquired with an exposure time of 250 µs, at a frame rate of 2 Hz. Each image was spatially binned (3×3 pixels, giving an effective pixel size of 63.3 nm/px) and sets of 10 recorded images were temporally binned to yield an effective frame rate of 0.2 Hz (one saved image every 5 s). We note that, while this acquisition speed is relatively slow compared to what can be achieved using iSCAT,[53] it is sufficient to capture the phase transitions occurring in our experiments. To avoid saturation of the detector, the power of the laser was reduced by lowering the repetition rate to 4 MHz and setting the driver current just above the turn-on threshold, resulting in a measured power of < 1 mW before entering the objective. At this power, no sample degradation was observed.

Experiments presented in Figure 4 (and Figure 1f, Extended Data Figure 1f-i) were carried out using similar powers at a repetition rate of 5.3 MHz. The camera exposure time was set to 1 ms and each recorded image was spatially binned (4×4, giving 117 nm/px). Images were recorded at effective frame rates of 0.5, 0.5, 1, 1 and 2 Hz for experiments with applied C-rates of C/2, 1C, 2C, 4C and 6C, respectively. In all experiments except at 6C, sets of 2 images were temporally binned to yield the stated effective frame rate, while no temporal binning was employed at 6C.

Galvanostatic control of the sample was achieved using a portable potentiostat (SP-200, BioLogic). The cell rested at the open-circuit voltage for at least 20 min prior to each experiment. For the experiment presented in Figures 2, 3, and 5, a constant current of 0.1525 mA (2C) was applied during cycling, with a voltage range of 3 – 4.2 V (vs. Li^+/Li). Upon reaching the upper voltage threshold of 4.2 V during charging, the direction of current was inverted. The cell was then discharged until reaching the lower voltage threshold of 3 V. This was repeated for five consecutive cycles, which showed no noticeable differences in their electrochemical performance. For the investigation into C-rate dependence presented in Figure 4, two consecutive galvanostatic cycles were completed for each C-rate (C/2, 1C, 2C, 4C, 6C), with a voltage range of 3 – 4.3 V (vs. Li^+/Li).

4. Data Analysis

Jitter correction and background subtraction

All recorded image stacks were first corrected for jitter in the *xy*-plane by isolating a bright sub-diffraction limited spot (unrelated to the active particle) and fitting its position over time

using a two-dimensional Gaussian function. The extracted centre positions in *x* and *y* for each image were subsequently used to correct for stage drift.

Background-subtracted images are shown in Figure 2b and in Supplementary Videos 1 and 6-10. To obtain these, the average image over 100 frames prior to electrochemical cycling was subtracted from each of the remaining frames, to allow direct comparison of the intensity variations across the particle. Finally, the entire image stack was normalised to a linear intensity scale with a range of 1.

Differential image analysis

The normalised sequential differential images shown in Figure 5e,f were obtained by dividing the $(i+1)^{th}$ frame by the i^{th} frame, and then subtracting 1. The resulting image contrast displays the fractional intensity change over the duration of 5 s (*i.e.* between subsequent frames), with the contrast scale centred around 0. This removes slowly varying background contributions and inhomogeneities in the sample illumination to isolate more rapid changes between the images. The sequential differential images shown in Figure 3a,b were calculated using the $(i+4)^{th}$ frame and the i^{th} frame, to represent intensity changes over a 20 s duration (*i.e.* 4 frames).

Normalised total differential images (Figure 5a,b) were calculated similarly to the sequential differential images. Here, we took a frame from just after the completion of the transition, divided it by another frame from just before the transition, and then subtracted 1. These images therefore represent the fractional intensity change for each pixel over the entire duration of the transition.

The differential images were additionally masked for clarity to exclude regions that are not part of the active particle. To accomplish this, the unprocessed image from Extended Data Figure 1e was used to generate a binary mask whereby all pixels with a normalised intensity value below 0.23 were set to 0.

Phase fraction and single-particle C-rate calculation

The phase fractions shown in Figure 3c,d were extracted from masked sequential differential images (obtained from consecutive i^{th} and $(i+1)^{th}$ frames). A temporal window of 1000 s, containing the relevant insulator-metal biphasic phase transition, was first selected from the differential image stack. Here, each pixel's time-domain response exhibits a short oscillatory feature associated with the moving phase boundary. A short-window Fourier transform (SWFT) algorithm was used to identify the time at which the phase boundary passed

over each pixel in the image. The SWFT algorithm was applied with a Hanning window (160 s width, selected to give the best time-frequency resolution), and the window time at which the Fourier spectrum showed a global maximum was recorded. This time-point was taken to be the time when the phase boundary travelled across the given pixel. Due to residual noise contributions, some pixels do not have a well-defined spectral features in the SWFT, but instead exhibit peaks at DC or Nyquist frequencies. To remove these pixels, a maximum-frequency histogram was constructed for all pixels and only pixels which showed a maximum amplitude between 5 and 83 mHz were included in further analysis (~90% of all pixels). By counting the pixels that had already experienced the phase boundary at each moment and normalising for the overall particle area, we were able to derive the phase fractions as a function of time. Finally, we assumed that rejected pixels were filled according to the underlying phase fraction dynamics, allowing us to scale the resulting curves to achieve full coverage by the new phase. This procedure was applied for all cycles.

The corresponding biphasic single-particle C-rates were obtained from the time derivative of the new phase fraction and scaled to the relevant capacity units. The scaling factor is 1268 s, which is the time taken for the lithium content in Li_xCoO_2 to change by $\Delta x = 0.18$ at 1C. This value of Δx corresponds to the miscibility gap between $Li_{0.95}CoO_2$ and $Li_{0.77}CoO_2$, see Supplementary section 5.

A similar analysis was carried out for the results shown in Figure 4b,c. Here, sequential differential images were first computed (from consecutive i^{th} and $(i+1)^{th}$ frames) and image stacks containing the insulator-metal biphasic transitions were generated. Subsequently, we temporally binned sets of 10 differential images. A SWFT algorithm (Hanning window with width equivalent to the time duration of the image stack) was then used to extract the time-dependent phase fraction and single particle C-rates, after rejecting pixels associated with DC and Nyquist frequencies (leaving >80% of all pixels), as explained above.

The time-maps presented in Figure 4d were generated by plotting the time at which each pixel experienced the phase boundary, as determined by the SWFT algorithm, and normalising to the overall time range of the biphasic transition. This allows the propagation of the phase boundary over the full duration of the transition to be visualised in a single image. Since it can be assumed that any rejected pixels follow the underlying behaviour of the phase transition, we apply an 'inpainting' algorithm to interpolate to their expected transition times, which we include in the time-map images. We also refer the reader to Supplementary Videos 6-10, including the relevant transitions.

Additional references for methods

53. Spindler, S. *et al.* Visualization of lipids and proteins at high spatial and temporal resolution via interferometric scattering (iSCAT) microscopy. *J. Phys. D: Appl. Phys.* **49**, 274002 (2016).

Acknowledgements

The authors acknowledge financial support from the Faraday Institution, Battery Characterisation Call. A.J.M. acknowledges support from the EPSRC Cambridge NanoDTC, EP/L015978/1. C.S. acknowledges financial support by the Royal Commission of the Exhibition of 1851. We acknowledge financial support from the EPSRC and the Winton Program for the Physics of Sustainability. This project has received funding from the European Research Council (ERC) under the European Union's Horizon 2020 research and innovation program (Grant Agreement No. 758826). C.S. thanks Professor Philipp Kukura, Dr. Adam Fineberg and Dr. Gavin Young for helpful discussions during the initial phase of the project.

Author contributions

A.R. conceived the idea. A.R. and C.P.G. planned and supervised the project. C.S. designed the optical setup. Q.J. and A.J.M. prepared samples. C.S., Q.J. and A.J.M. planned all experiments and A.J.M. carried out the measurements. Q.J. developed the phase field modelling. All authors discussed the results and contributed to writing the manuscript.

Competing interests

The authors declare no competing interests.

Additional information

Supplementary Information is available for this paper.

Correspondence and requests for materials should be addressed to:

Christoph Schnedermann – cs2002@cam.ac.uk

Clare P. Grey – cpg27@cam.ac.uk

Akshay Rao – ar525@cam.ac.uk

Data availability

The data underlying all figures in the main text and Supplementary Information are publicly available from the University of Cambridge repository at [url to be added in proof]

Code Availability

All code used in this work is available from the corresponding author upon reasonable request.

Extended data figures

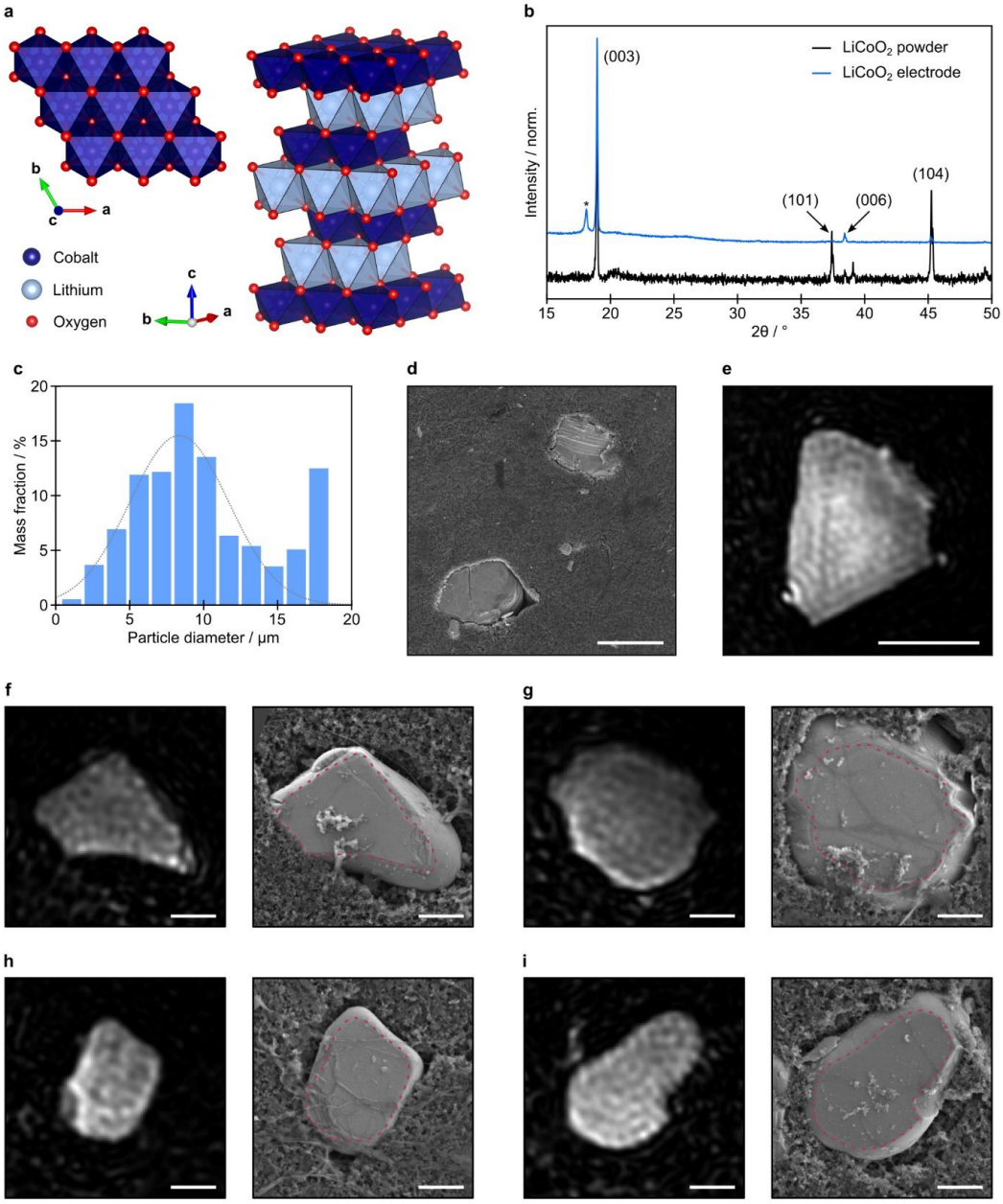

Extended Data Figure 1: Structure and orientation of LCO particles, and comparison of iSCAT and scanning electron microscopy (SEM) images.
a Crystal structure of $LiCoO_2$. Upper left: View down the *c*-axis, showing edge-sharing CoO_6 octahedra. Right: Angled view showing alternate layers of cobalt-centred and lithium-centred octahedra. Four unit cells are displayed (two repeats in the *a*- and *b*-directions). Lithum transport occurs in the *ab*-plane. **b** X-ray diffraction patterns of the pristine LCO powder (black) and self-standing electrode film (blue). The comparatively high intensities of the (00l) reflections indicate that the LCO particles display a preferred orientation within the electrode film, with the [001] direction (*i.e.* *c*-direction) normal to the electrode film. The peak marked * originates from the conductive carbon. **c** Mass-weighted diameter distribution for LCO particles (based on 681 particles). **d** SEM image of a dilute working electrode, showing two particles of LCO dispersed in a conductive matrix. Scale bar is 10 µm. **e** iSCAT image of a single active LCO particle in the electrode (250 µs exposure time). Intensity values are normalised normalised to a linear scale between 0 (black) and 1 (white). Scale bar is 5 µm. **f-i** Left: iSCAT intensity

image of a LCO particle, normalised between 0 (black) and 1 (white). Right: Corresponding SEM image of the same LCO particle. The red dashed line represents the outline of the bright region in the iSCAT image. All scale bars are 2 μm. Comparisons of iSCAT and SEM images confirm that the bright regions observed by iSCAT correspond to relatively flat areas on the particle surface. The curved sides of each particle are out of focus, and do not contribute significantly to the iSCAT image (Supplementary section 2). The flat surfaces imply that, for these particles, the direction of observation is along the *c*-axis of the crystal. This particle orientation is ideally suited to investigate the in-plane ion transport within the layered host lattice.

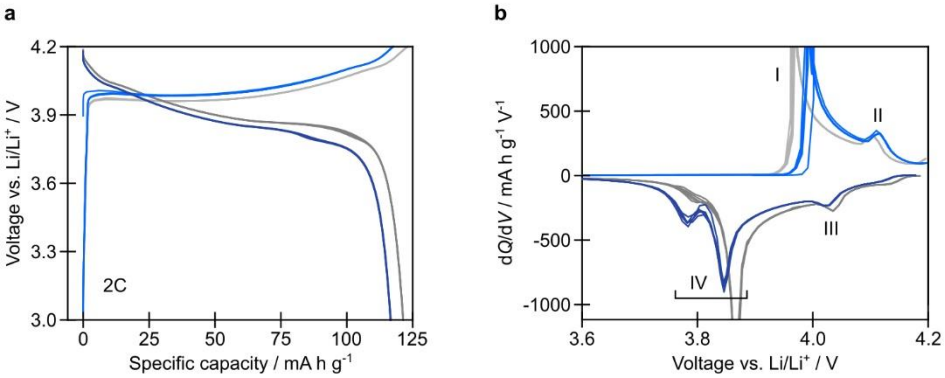

Extended Data Figure 2: Galvanostatic cycling (2C) of LCO in an optical cell and a coin cell. **a** Specific capacity plots for 5 cycles of LCO electrodes in the optical cell (blue, as shown in Figure 1b,c) and in a coin cell (grey), each cycled at a rate of 2C from 3.0 – 4.2 V. **b** Corresponding differential capacity plots. The positive absolute value of d*Q*/d*V* is displayed for delithiation, and the negative absolute value is displayed for lithiation. Peaks attributed to the biphasic transitions (I and IV) and lithium ordering (II and III) are indicated. Both cells were cycled ~20 times at 2C prior to obtaining the displayed data. The sets of results are in good agreement with each other and with previous reports for LCO.[16] The slightly higher overpotentials and lower capacity seen in the optical cell compared to the coin cell were likely caused by a higher internal resistance in the optical cell, perhaps due to the lower stack pressure.

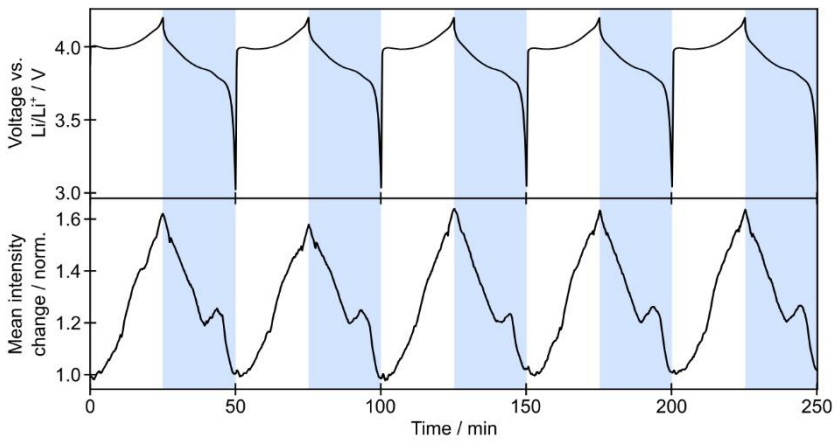

Extended Data Figure 3: Optical response of a LCO particle over five galvanostatic cyles (2C). Top: Cell voltage (vs. Li/Li^+) during five galvanostatic cycles at 2C (as plotted in Figure 1b,c), as a function of time. Bottom: iSCAT intensity change averaged over the active particle shown in Extended Data Figure 1e, during this galvanostatic cycling. White and blue vertical bars indicate delithiation (charging) and lithiation (discharging), respectively.

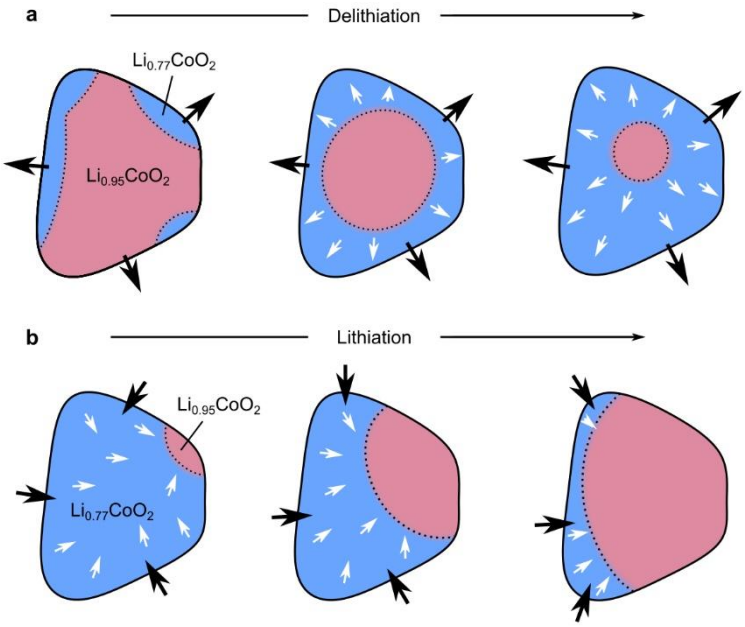

Extended Data Figure 4: Schematic showing biphasic mechanisms upon delithiation and lithiation.

a Shrinking core mechanism upon delithiation. **b** Intercalation wave mechanism upon lithiation. Throughout, the lithium-rich phase ($Li_{0.95}CoO_2$) is represented in pink and the lithium-poor phase ($Li_{0.77}CoO_2$) is in blue. Black arrows indicate the direction of lithium-ion transport at the particle surface (*i.e.* charge transfer), and white arrows indicate lithium-ion diffusion in the bulk particle.

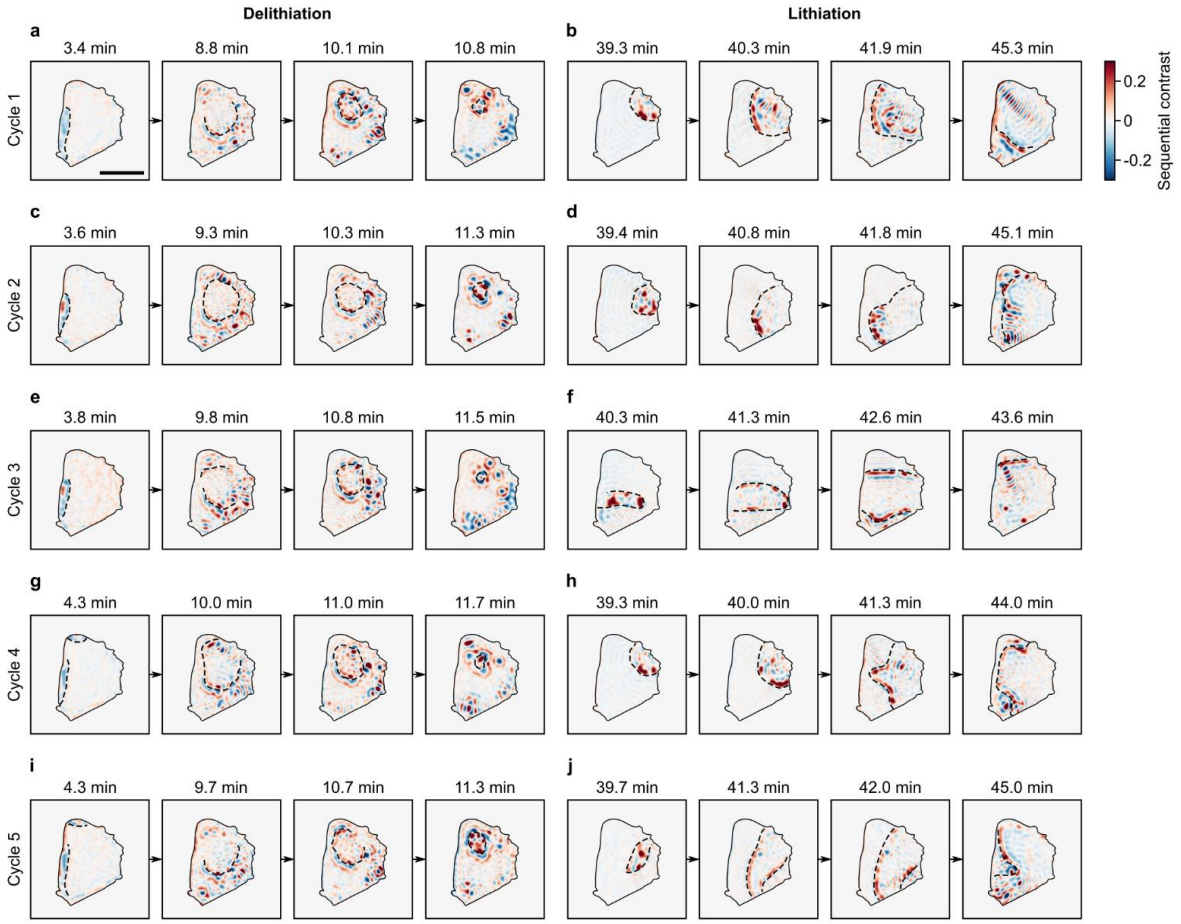

Extended Data Figure 5: Behaviour of biphasic transitions upon (de)lithiation for all five cycles. Sequential differential images of the active particle upon delithiation (a,c,e,g,i) and lithiation (b,d,f,h,j) during the biphasic transition, for all five galvanostatic cycles. The black dashed lines are a guide for the eye, representing the phase boundary position. Sequential contrast represents the intensity changes over a 20 s timescale, and the colour-scale is consistent throughout all images. Scale bar is 5 µm.

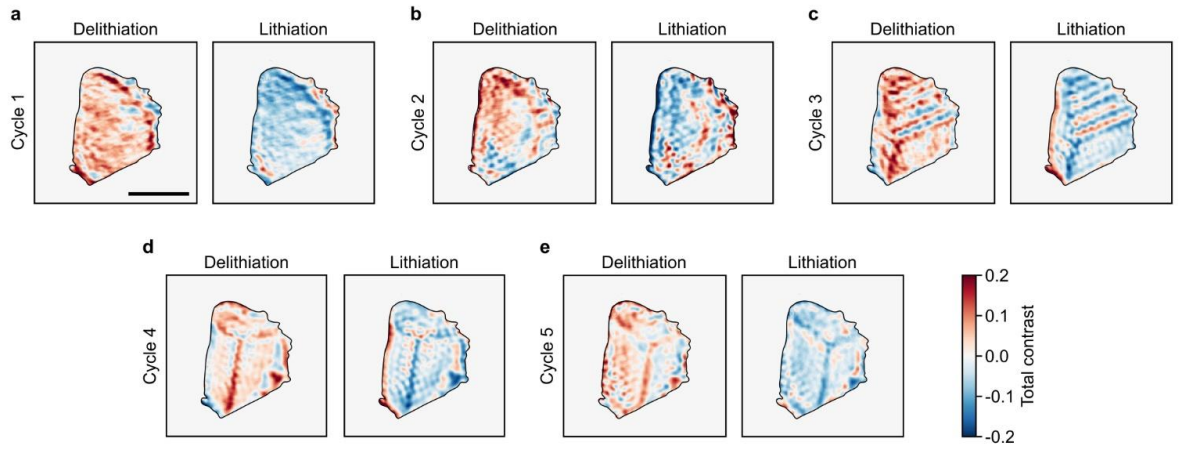

Extended Data Figure 6: Intensity changes caused by ordering transitions upon (de)lithiation for all five cycles.
Images showing the total contrast resulting from lithium ordering for delithiation and lithiation, for all five galvanostatic cycles. These represent the total intensity change caused by the transition, and the colour-scale is consistent throughout all images. For cycles 3, 4 and 5, the formation of the ordered state produces bright lines at approximately 120°. Scale bar is 5 µm.

Supplementary Information for

Operando optical tracking of single-particle ion dynamics in batteries

Alice J. Merryweather[1,2], Christoph Schnedermann[1]*, Quentin Jacquet[2], Clare P. Grey[2,]* & Akshay Rao[1,]*

[1] Cavendish Laboratory, University of Cambridge, J. J. Thomson Avenue, Cambridge CB3 0HE, United Kingdom

[2] Department of Chemistry, University of Cambridge, Lensfield Road, Cambridge CB2 1EW, United Kingdom

Contents

1. iSCAT signal contributions for LCO

The components contributing to iSCAT intensity ($\mathbf{E}_s$ and $\mathbf{E}_r$) are illustrated in Figure 1e and described briefly in the main text. For our work, since the single-crystal LCO particles are much larger than the illumination wavelength, $\mathbf{E}_s$ is dominated by reflection of light at the electrolyte/LCO particle interface, with minor scattering contributions from surface roughness. The reference contribution, $\mathbf{E}_r$, originates from reflected light at the glass window/electrolyte interface and contains no information about the sample. The imaged iSCAT intensity is the result of interference between $\mathbf{E}_s$ and $\mathbf{E}_r$, giving rise to a detected intensity, I, according to:

$$I = |\mathbf{E}_r + \mathbf{E}_s|^2 = |\mathbf{E}_r|^2 + |\mathbf{E}_s|^2 + 2|\mathbf{E}_r||\mathbf{E}_s|\cos(\Delta\phi), \quad (1.1)$$

where $\Delta\phi$ denotes the phase difference between $\mathbf{E}_r$ and $\mathbf{E}_s$.[1] The third term in the above equation corresponds to the interference of $\mathbf{E}_r$ and $\mathbf{E}_s$. Due to its linear dependence on $|\mathbf{E}_s|$, this term is sensitive to small changes in the scattering properties of the sample.[1-4] The path length difference between $\mathbf{E}_r$ and $\mathbf{E}_s$ additionally produces an inversion in the sign of this interference term over a distance of $\lambda/4$ (where λ is the illumination wavelength) in the axial direction. For the illumination wavelength used in this work, the distance of $\lambda/4$ is less than the axial depth of field of the microscope (see Supplementary section 2), and so this intensity oscillation will reduce the obtained iSCAT contrast due to destructive interference contributions.[1,2] Due to the large thickness of the studied particles compared to illumination wavelength, precise quantitative analysis of the detected intensity is therefore non-trivial, and beyond the scope of this work.

The elastically scattered field $\mathbf{E}_s$ is directly related to the polarisability of the valence/conduction electrons in the sample material via

$$\mathbf{E}_s = \eta\alpha\mathbf{E}_i, \quad (1.2)$$

where $\mathbf{E}_i$ denotes the incident field, α is the polarisability and η is the collection efficiency of the detection system. For electrode materials, changes to the electronic structure during (de)lithiation affect the polarisability of the material, and thus change the amount of light that is scattered and the detected iSCAT intensity. For example, as shown in Figure 2a, the average iSCAT intensity for a particle of LCO increased by 1.6 times its original value during delithiation, followed by an equivalent decrease upon lithiation. Upon delithiation, the conduction band becomes increasingly occupied with electrons.[5] Therefore, the degree of electronic delocalisation progressively increases, resulting in a larger polarisability, α. Since $\mathbf{E}_s \propto \alpha$, this gives rise to a higher scattering intensity as more lithium-ions are removed. The reverse process occurs on lithiation, causing the polarisability of the material and the iSCAT

intensity to reduce again. We note that more detailed studies would be required to determine the lithium concentration quantitatively in LCO directly from the iSCAT intensity values, by determining the optical properties of the material at every composition. Such optical properties can often be computed by DFT-based methods.

2. Discussion of imaging depth

To understand how deep into the sample the presented iSCAT setup can resolve features, we examine i) the depth of field and ii) the penetration depth of light in the LCO particle. The depth of field describes the distance along the optical axis over which an imaged object produces a sharp image on the camera. The depth of field in an optical microscope can be calculated from the incident wavelength (λ) and the numerical aperture (NA) of the objective, according to

$$d = \frac{n\,\lambda}{2\,\mathrm{NA}^2} + \frac{n}{M\,\mathrm{NA}}e, \quad (2.1)$$

where n is the refractive index of the medium between the objective and coverslip, M is the overall magnification of the imaging system and e is the pixel size of the camera. In our case, an immersion oil with n = 1.518, a wavelength of λ = 780 nm and a NA = 1.4 objective give a depth of field of ~330 nm. This implies that any object within 330 nm of the chosen focal plane will give rise to an 'acceptable' focused image on the detector.

This shallow depth of field explains the difference between iSCAT and SEM images represented in Figure 1f and Extended Data Figure 1f-i. Here, iSCAT images identify the flat surfaces of the examined particles. Features occurring at deeper sample depths, such as the curved sides of the particles visible in the SEM images, are not visible since they are beyond the depth of field. These out-of-focus features give rise to a non-zero blurred background intensity superimposed onto of the particle image. Since the particles investigated here are embedded in a highly scattering carbon matrix, this background contribution is overwhelmed by a strong speckle pattern originating from the carbon. During operando measurements, the appearance of phase boundaries will appear 'sharp' only when resolved within the depth of field. Conversely, any phase boundaries outside the depth of field will be blurred, resulting in reduced contrast and a broadened spatial profile.

The effective penetration depth of light can be affected by the absorption properties of the studied material. For LCO, previously reported spectro-ellipsometry studies of pristine, single-crystalline Li_xCoO_2 particles (x = 0.87) estimate an optical absorption coefficient at 780

nm of ~4×10^{-4} cm^{-1},[6] corresponding to an absorption depth of ~250 nm (*i.e.* the depth at which the incident intensity is reduced to 1/e its initial value).

Overall, for LCO, both the depth of field and the absorption limit the depth at which features can be resolved to ~300 nm. The LCO particles pictured in Figure 1f and Extended Data Figure 1e-i are oriented such that the optical axis is normal to flat areas of the particle, which correspond to the (001) surface. For particles which are oriented in this way, iSCAT can track the two-dimensional ion transport in this plane, for layers close to the particle surface according to the depth of field and the absorption. Taking a *c*-lattice parameter of 14.04 Å for LCO, our iSCAT studies are therefore most sensitive to phase boundaries occurring within ~214 unit cell layers of the surface.

3. Localisation precision for phase boundaries

The 'localisation precision' describes the precision to which the position of a feature (such as a phase boundary) can be determined in our iSCAT images. We emphasise that localisation precision is not equivalent to 'resolution'. Lateral resolution describes the length scale over which features can be spatially distinguished in an image, and is proportional to the illumination wavelength. For our microscope (λ = 780 nm, NA = 1.4), the lateral resolution is ~280 nm (full width at half-maximum, FWHM). Nevertheless, it is possible to track the position of a mobile feature with a well-defined centre-of-mass to a higher localisation precision, by determining the centre-point of the intensity feature. This localisation precision is independent of the illumination wavelength, and is instead determined by the signal-to-noise ratio of the image.[7–10]

We determined typical values of the localisation precision for a moving phase boundary during the biphasic transition, for the data set presented in Figure 2 (and Supplementary Video 1). For both delithiation and lithiation, we first computed sequential differential images (from consecutive i^{th} and $(i+1)^{th}$ frames) and selected a set of frames containing the moving phase boundary. We then took a representative line-cut across the image stack, perpendicular to the direction of phase boundary movement. For each frame, the phase boundary appears in the line-cut as a positive contrast peak, with smaller oscillatory contrast features on each side. The position of the phase boundary in each frame can therefore be found by fitting a one-dimensional Gaussian curve (using a χ^2 fitting algorithm) to the central positive contrast peak, to determine its centre-point. The achieved localisation precision is then represented by the mean of the uncertainties associated with these fitted centre-points (as obtained from the

covariance matrix), across the whole set of frames. The resulting localisation precision values were 2.7 ± 0.4 nm for delithiation (based on a set of 21 frames) and 3.8 ± 0.3 nm for lithiation (based on 32 frames). As such, our iSCAT methodology is capable of determining the position of moving phase boundaries with a precision of sub-5 nm.

4. Method of extracting phase boundary velocity

To obtain values for the phase boundary speed upon delithiation (using the data presented in Figure 2 and Supplementary Video 1), a narrow rectangular region (0.9 × 4.5 μm) of the background-subtracted image stack was selected such that the phase boundary moved through it, parallel to the long direction of the rectangle (Supplementary Figure 1a). Intensity values were averaged across the short direction of the rectangle to produce a one-dimensional intensity profile for each frame, in which the phase boundary is visible as an intensity oscillation with a central bright feature. These intensity profiles are plotted for the relevant duration of the biphasic transition (for cycle 1) in Supplementary Figure 1b. The bright feature was taken to be the location of the phase boundary, and the position of its centre was found for each frame by fitting a one-dimensional Gaussian function. Supplementary Figure 1c shows the resulting distances travelled by the phase boundary over time, for all five cycles. This corresponds to phase front velocities of 10 – 37 nm s^{-1}, with an average of ~20 nm s^{-1}.

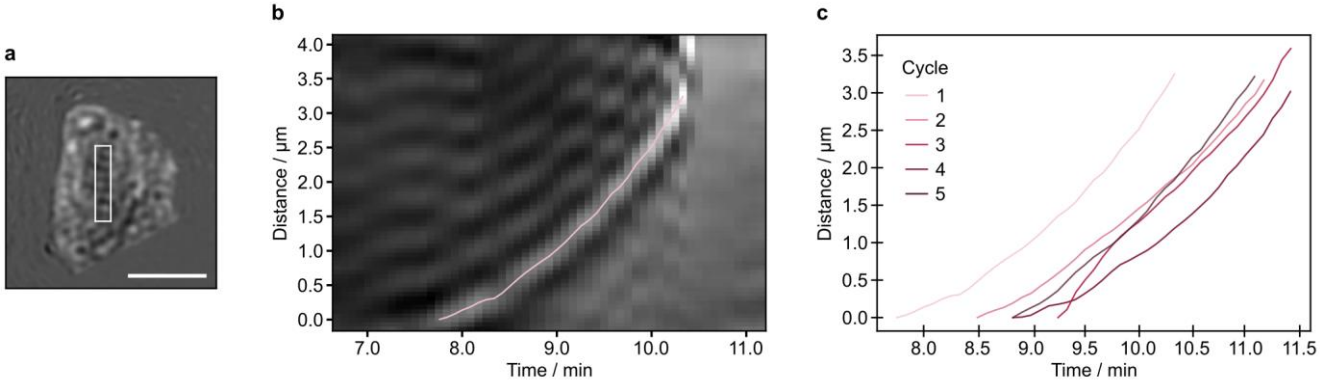

Supplementary Figure 1: Method of extracting values for phase boundary speed during delithiation.
a Background-subtracted image of a LCO particle during the biphasic transition upon delithiation. The white reactangle shows the region used to calculate phase boundary speeds. Scale bar is 5 μm. **b** One-dimensional intensity profiles plotted for each frame (*i.e.* over time) during the relevant part of the biphasic transition, for cycle 1. The intensity values are scaled between 0 (black) and 1 (white). The pink line represents the fitted position of the phase boundary. **c** Evolution of the position of the phase boundary within the rectangle region, for all five cycles. Time is given relative to the start of the cycle.

5. Limiting compositions of the insulator-metal biphasic transition in LCO

For Li_xCoO_2, the limits of the solid solution regimes on either side of the insulator-metal biphasic transition are typically reported as $x \approx 0.95$ and $x \approx 0.75$.[11] However, highly stoichiometric LCO samples, with a very low concentration of defects have been shown to have a wider immiscibility gap, with the biphasic transition starting as early as the $Li_{0.99}CoO_2$ composition.[12] Therefore, the miscibility gap of the biphasic transition can vary depending on the precise material stoichiometry.

To determine the size of the miscibility gap for the LCO used in this work, we performed an electrochemical experiment using the galvanostatic intermittent titration technique (GITT). An electrode was prepared by casting a slurry containing 80% LCO (with 10% Super P™ carbon, 10% polyvinylidene fluoride) onto aluminium foil, and assembled into a coin cell with a Li metal counter electrode. The GITT experiment was performed by applying a series of C/5 current pulses, each lasting 5 minutes, with a 10-hour relaxation period between each pulse to allow the cell to reach its thermodynamic open circuit voltage (OCV). The results are displayed in Supplementary Figure 2. The duration of the insulator-metal biphasic transition is identifiable as a plateau where the OCV is constant. This plateau occurs between $Li_{0.95}CoO_2$ and $Li_{0.77}CoO_2$, giving the miscibility gap of the biphasic transition for our LCO electrodes. Therefore, throughout this work, $Li_{0.95}CoO_2$ and $Li_{0.77}CoO_2$ are taken to be the compositions of the coexisting phases during the insulator-metal biphasic transition.

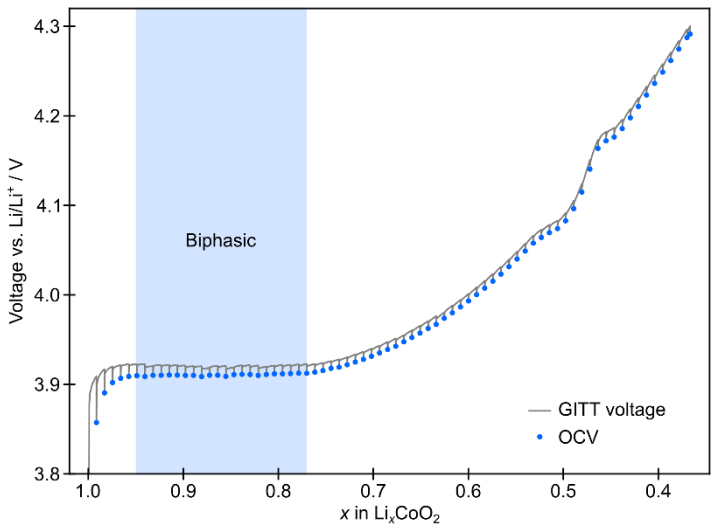

Supplementary Figure 2: Galvanostatic intermittent titration technique (GITT) for LCO. The cell voltage during a GITT experiment (C/5 current pulses applied for 5 minutes, each followed by 10 hour rest period) is shown in grey, as a function of the average composition of Li_xCoO_2 in the working electrode. The open circuit voltage (OCV) at the end of each 10 hour rest period is indicated by a blue dot. The blue shaded region highlights the OCV plateau corresponding to the metal-insulator biphasic transition ($0.95 > x > 0.77$).

6. Applicability of iSCAT to other materials

Since changes in iSCAT contrast originate from changes in the electronic polarisability of the sample, the operating principles are generalisable beyond LCO: as long as ionic motion is coupled to electronic changes, iSCAT has the potential to probe (de)intercalation dynamics universally. In addition to single-crystal active particles, iSCAT is applicable to particles with more complex morphologies and defect structures, opening an exciting potential area of investigation concerning the impact of defects and grain boundaries on ionic mobility and phase boundary formation and propagation. It is worth noting that the lateral resolution limit of our microscope (~280 nm, see Supplementary section 3) means that particles should ideally be larger than ~1 μm to be able to resolve spatial variations in intensity within a particle. For smaller particles, spatial resolution of features within the particle is limited, but intensity changes upon cycling would still be observable owing to iSCAT's high localisation precision of sub-10 nm (see Supplementary section 3). For example, when considering secondary particles made up of small agglomerated primary particles, it would be possible to track the progression of the (de)lithiation across the secondary particle, but not necessarily to resolve features within the primary particles of sub-μm size.

Lithiation and delithiation dynamics of $Nb_{14}W_3O_{44}$

In order to clearly demonstrate the universality of optical light scattering as a probe for single-particle ion transport dynamics, we present here preliminary results for $Nb_{14}W_3O_{44}$ (NWO), a high-rate anode material.[13,14] This material is a Wadsley-Roth crystallographic shear phase made up of block-type structures of NbO_6 and WO_6, and takes the form of large (multiple-μm) rod-like particles.

NWO electrodes were prepared and examined with *operando* iSCAT microscopy, using similar methods to those described for LCO. Supplementary Figure 3a shows optical images of a rod-like particle of NWO surrounded by the carbon matrix, at different stages of lithiation. A dramatic intensity increase to 1.7 times its original value was seen during cycling (at 1C). Therefore, as with LCO, significant changes to the electronic and dielectric properties[14] during electrochemical cycling of NWO allow optical monitoring of the lithiation and delithiation processes. Additionally, the physical expansion of the material as lithium-ions are inserted can be clearly observed in the long direction of the rods (corresponding to the crystallographic *c*-axis). Supplementary Figures 3b,c show the cell voltage alongside the mean particle intensity and optically observed *c*-axis expansion for this individual particle. The maximum expansion

of ~6% is consistent with previous diffraction literature,[13,15] smaller expansions being observed at higher C-rates, since less lithium is reversibly inserted. Future work will examine the (de)lithiation dynamics of NWO in more detail.

The dramatic changes in scattering intensity that are observed for both LCO and NWO highlights that optical scattering microscopy can be applied generally to many kinds of battery electrodes. Among others, this could include NMC, NCA, graphite and silicon.

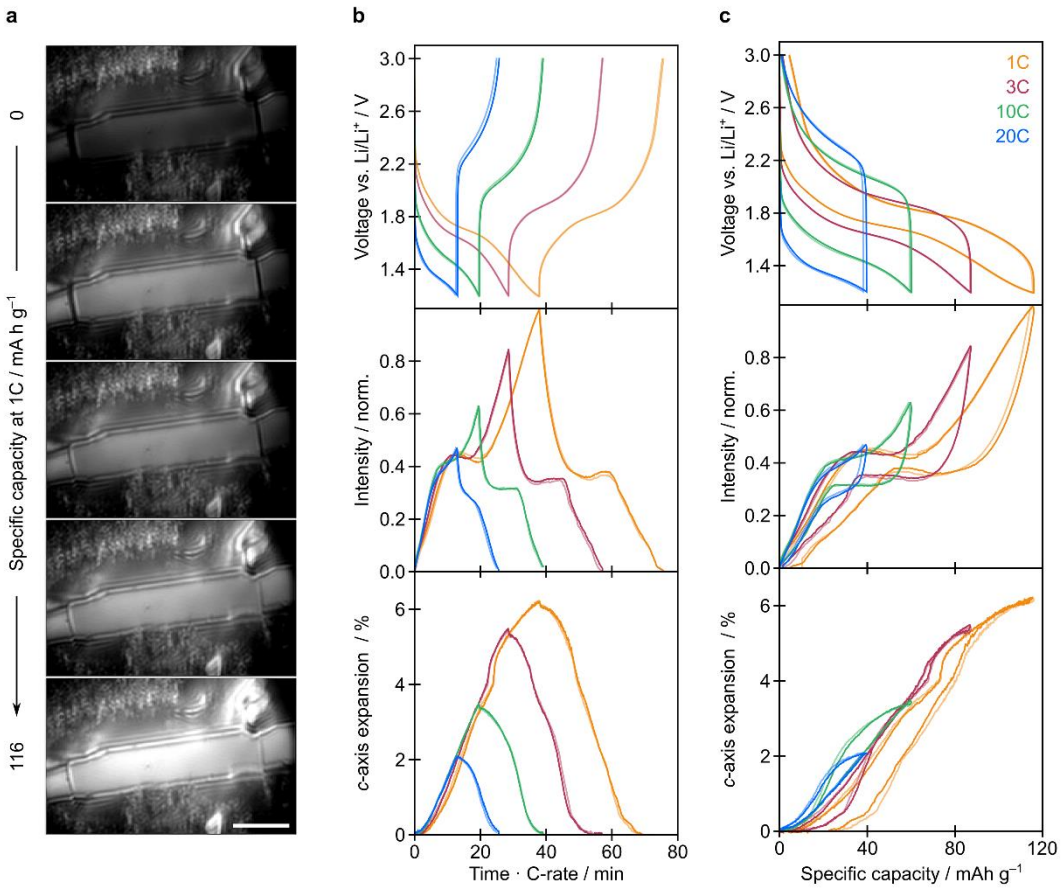

Supplementary Figure 3: Optical response of a NWO particle during galvanostatic cycling. **a** Optical scattering microscopy images of a rod-like particle of NWO, indicating the increasing scattering intensity during lithiation at 1C. Scale bar is 5 µm. **b, c** Top: Cell voltage (vs. Li/Li^+) during galvanostatic cycling at rates of 1C, 3C, 10C and 20C, in a voltage range of 1.2 – 3 V. Middle: Detected iSCAT intensity change averaged over the central rod-like particle, normalised to the maximum intensity at 1C. Bottom: Optically observed expansion along the length of the central rod-like particle (corresponding to the crystal *c*-axis). Panels b and c show equivalent data, plotted as a function of time and specific capacity of the cell, respectively. Two cycles are shown for each C-rate, with the second cycle plotted in a paler colour.

7. High rate and throughput capabilities of iSCAT

To establish the acquisition rate capabilities of our microscope in the context of LCO, we evaluate the signal-to-noise ratio (SNR) for a moving phase boundary feature in the data set displayed in Figure 3. This data was acquired with a 250 µs exposure time, applying 3 × 3

pixel binning, and temporally binning of sets of 10 consecutive frames. We select a series of frames containing a typical moving phase boundary, compute sequential differential images, and take a line-cut perpendicular to the phase boundary. Comparison of the peak-to-peak contrast of the phase boundary feature with that of the noise in the absence of such a feature yields a SNR of 11 ± 1 (average over 21 effective frames). Since the SNR is limited by shot-noise, a single frame acquired prior to the 10-frame temporal binning has a SNR of ~3.5. Reducing the exposure time from 250 μs to 140 μs would result in a SNR of ~2, which would still be sufficient to resolve the phase boundary feature. This 140 μs exposure time allows for frame rates potentially as fast as ~7000 Hz. The same SNR could be achieved with even faster acquisition times by increasing the illumination intensity. This highlights the high-rate capabilities and sensitivity of iSCAT when applied to systems such as LCO.

The fastest process we have observed in LCO is the lithium ordering transition, close to a composition of $Li_{0.5}CoO_2$, which (for the particle and data presented in Figure 5) lasted just 20 s during delithiation and 35 s during lithiation. We recorded phase boundaries moving at velocities of ~70 nm s^{-1} during these transitions. However, the sub-ms acquisition times and high sensitivities achievable with iSCAT opens up the possibility of studying even faster processes occurring in battery systems, which are especially difficult to access with other techniques. For example, this could include the nucleation process of new phases, formation of surface species, and ion diffusion in solid electrolytes.

The high-rate capabilities of iSCAT may also be beneficial for the pursuit of extreme fast charging (XFC) batteries. These are important to the development of more desirable electric vehicles, for example, achieving targets such as the ability to charge a battery pack to 80% of its capacity within 15 minutes.[16] Fast charging may be limited not only by rate of ion transport through active materials, but also through the electrolyte and at interfaces, as well as by electronic conductivities. To optimise charging rates, it is therefore important to identify what these limiting processes are. Particularly at fast cycling rates, iSCAT promises to be a useful tool to identify rate-limiting processes and to evaluate the effectiveness of attempts to improve them, including the effects of particle coatings and electrode tortuosity.

Importantly, the iSCAT methodology enables a high-throughput of single particle measurements. The straightforward setup and sub-ms image acquisition times mean that the duration of the electrochemical cycling limits the rate at which experiments can be performed. However, with this presented set-up, and these dilute electrodes, to examine particles across multiple fields of view, the cell must be cycled multiple times. This works well for materials

with high reversibility, but might be more challenging for materials that exhibit significant capacity fade. Future improvements of our methodology will therefore employ a larger field of view, to enable multiple individual particles to be imaged simultaneously. This could be achieved without loss of resolution by matching the field of view to a 25 mm sensor with 60× magnification, to allow observation of a 0.4 × 0.4 mm area at 100 Hz image acquisition rates, enabling imaging of > 400 particles per field of view. Using modern stitching techniques, the number of imaged particles could be increased by another factor of 10-50 without loss of dynamic information.

8. Comparison with alternative *operando* imaging methods

Supplementary Table 1 compares the key characteristics and limits of *operando* imaging techniques (with sub-µm resolution) commonly employed in battery research with those of iSCAT. In general, the fast acquisition times, low sample damage, and relatively straightforward implementation offered by optical microscopy (including iSCAT) make it well suited for many *in situ* and *operando* applications[17–20] in the field of battery materials.

Supplementary Table 1: Comparison of *operando* imaging techniques employed in lithium-ion battery research.
(TEM = transmission electron microscopy, SEM = scanning electron microscopy, TXM = transmission X-ray microscopy, EDX = energy-dispersive X-ray spectroscopy, EELS = electron energy loss spectroscopy, XANES = X-ray absorption near edge structure). *Electrochemical cells suitable for lithium-ion battery experiements are not commercially available to the best of our knowledge at the time of publication. †Note that the interferometric signal contribution undergoes a sign inversion over a distance of $\lambda/4$ in the axial direction, as discussed in Supplementary section 1.

	In-situ TEM	*In-situ* SEM	TXM	Scanning confocal Raman microscopy	iSCAT
Radiation or illumination	Electrons	Electrons	X-rays	Visible light (typ. 400-900 nm)	Visible light (typ. 400-700 nm)
Imaging beam energy	10 keV - 1 MeV[23]	500 eV - 30 keV[21]	250 eV - 50 keV[23]	> 1 mW	< 1 mW
Operating principle for contrast formation	Absorption or diffraction of electrons (particularly by heavy atoms) provides information about atomic arrangements and detailed crystallographic information. Can be combined with EDX or EELS for elemental analysis and oxidation state/ local structure information.[21]	Electrons originating from the sample surface are detected, providing information about morphology and surface structure. Can be combined with EDX for elemental analysis.[25]	Typically uses absorption contrast, where images represent the density of electrons capable of absorbing the relevant X-ray energy. Can be combined with XANES analysis for elemental mapping and structure/oxidation state information, computed tomography for 3D analysis, or diffraction for crystallographic information.[23,24]	Spectrally resolved (inelastic) Raman scattering provides information about vibrational modes in the sample. Spatially-resolved hyperspectral images can be achieved by scanning a focused beam over the sample area.[21]	Scattering contrast depends on polarisability/ dielectric properties of the sample. Contrast is therefore sensitive to the electronic structure of the sample. For example, this can vary as a result of changing material composition or electronic conductivity.
Typical lateral resolution	Atomic resolution to nm resolution[21,23]	Typically < 10 nm[21]	~25 nm[21–23]	~ 250 nm	~ 200-300 nm (with sub-5 nm localisation precision during dynamic imaging)
Typical image acquisition times	Several seconds to minutes	Several seconds	Typically ~1 s (synchrotron source) or ~1 min (lab source) for full-field methods.[23] Longer for scanning images, *e.g.* to include diffraction, elemental mapping or tomography.	Seconds to hours, depending on Raman cross-section and imaged area[21,22]	Sub-ms
Penetration depth	< 1 µm. Beam must penetrate through entire sample.[23]	Surface sensitive, < 100 nm.[22]	10 - 100s nm (soft X-rays) or 5 µm - mm (hard X-rays).[23,25] Beam penetrates through entire sample.	Degree of surface sensitivity determined by depth of focus and optical properties of the sample. Typically ~ 300 nm.	Degree of surface sensitivity determined by depth of focus and optical properties of the sample. Typically ~ 300 nm.[†]
Sample requirements for *operando* imaging of lithium-ion batteries	Active material only. Open/closed (SiN_x window) cells with a non-volatile/volatile electrolyte.[21,25,28] Assembly of batteries and electrodes is non-trivial.	Open[26] cells with a non-volatile electrolyte.[21,25,27] Commercial cells not currently available*.	Full electrode (active material, carbon, binder) possible.[24] Commercial cells not currently available*.	Full electrode (active material, carbon, binder) possible. Commercial cells available.	Full electrode (active material, carbon, binder) possible. Commercial cells designed for other techniques (Raman) can be used.
Imaging conditions	Under vacuum	Under vacuum	Ambient temperature and pressure. Can be extended by adapting sample cell.	Ambient temperature and pressure. Can be extended by adapting sample cell.	Ambient temperature and pressure. Can be extended by adapting sample cell.

9. Phase field modelling:

(i) Methods

Classical modelling based on Fickian diffusion is not suitable to simulate lithium concentration profiles in LCO as it fails to reproduce the insulator-metal biphasic transitions, during which the $Li_{0.95}CoO_2$ and $Li_{0.77}CoO_2$ phases coexist at equilibrium. Instead, phase field modelling can be employed, as previously been shown with success for lithiation reactions of $LiFePO_4$ and TiO_2.[29–32] .

In a phase field model, the evolution of x (for Li_xCoO_2, $0 < x < 1$) is controlled by the gradient of a free energy functional, $G(x)$. The value of x is directly related to the lithium concentration, C_{Li}, (in mol m^{-3}) by

$$C_{Li} = x\, C_{max} , \qquad (9.1)$$

where C_{max} is the maximum amount (in mol m^{-3}) of Li per unit volume in Li_xCoO_2 (see Supplementary Table 2 for values of constants). The free energy, $G(x)$, of a single crystal of volume V is given by the Cahn-Hillard equation,[33]

$$G(x) = \int_V \left(g_h(x) + \frac{1}{2}\kappa \left|\nabla x\right|^2 \right) \mathrm{d}V . \qquad (9.2)$$

Here, $g_h(x)$ is the homogenous free energy of the single phase Li_xCoO_2 (in J m^{-3}), which is expressed in this work using the Redlich-Kister equation as proposed by Nadkarni *et al.*[34,35] The gradient energy coefficient, κ, used in the simulation is given by $\kappa/\mathrm{d}y^2 = 3.31 \cdot 10^8$ J m^{-3} (where dy is the mesh size). Further explanation of the choice of $g_h(x)$ and κ are given below.

The definition of the free energy enables the calculation of the lithium chemical potential, μ, (in J m^{-3}) which in turn defines the lithium flux, $\mathbf{j}$, (in m^{-2} s^{-1}) following

$$\mu = \partial G/\partial x , \qquad (9.3)$$

$$\mathbf{j} = -\frac{D(x)}{RT}\nabla\mu . \qquad (9.4)$$

Here, R is the gas constant, T is the temperature, and $D(x)$ is the lithium concentration dependent self-diffusion coefficient (in m^2 s^{-1}). Unless otherwise specified, we use a previously reported expression (9.5) for $D(x)$[35] (derived from a kinetic Monte Carlo approach by Van der Ven *et al.*[36]):

$$\log\left(\frac{D(x)}{a}\right) = b + cx + dx^2 + ex^3 , \qquad (9.5)$$

where the values of constants are specified in Supplementary Table 2. Note that $D(x)$ is the diffusion coefficient in the (00l) plane of the rhombohedral structure while the diffusion coefficient in the [00l] direction is taken to be zero.

At the particle surface, the lithium flux, **j**, is defined by a Butler-Volmer equation,

$$\mathbf{n}.\mathbf{j} = k_0 {C_{\mathrm{el}}}^{\alpha} \left((x-1)C_{\max}\right)^{\alpha} \left(xC_{\max}\right)^{\alpha} \left(\exp\left(-\frac{\alpha\eta F}{RT}\right) - \exp\left(\frac{(1-\alpha)\eta F}{RT}\right)\right) \quad (9.6)$$

as proposed by Doyle *et al.*[37] Here, **n** is the normal vector, α is the charge transfer coefficient, k_0 is the kinetic rate constant, C_{el} is the lithium concentration in the electrolyte, F is the Faraday constant, and η is the overpotential (in V). The overpotential is defined according to

$$\eta = \mu/F - \Phi\,, \quad (9.7)$$

where Φ is the electrode voltage (or the difference between the electrode and electrolyte potentials, in V).

Under galvanostatic conditions, the lithium flux at the surface is determined by the imposed current, I, (in A) according to

$$I = F\int_{\text{Active surface}} \mathbf{n}.\mathbf{j}\ \mathrm{d}A\,. \quad (9.8)$$

Note that surfaces perpendicular to the [00l] direction are not considered to be active surfaces.

The equations given above were solved using a finite element method implemented in MATLAB. The system under consideration was an 8×6×5 μm (X×Y×Z) rectangular parallelepiped of LCO, with a mesh size of 400 nm, and with the Z-direction being perpendicular to the crystal layers (*i.e.* the [00l] direction). This basic shape was chosen simply to explore the effect of lithium-ion transport and interfacial energies on the intercalation mechanisms. This system size was chosen such that its area in the XY-plane was similar to the particle observed by iSCAT (Supplementary Figure 4).

At this stage, we emphasise that we have considered the (de)lithiation mechanism of LCO to be two-dimensional, due to the anisotropic lithium diffusion and the presence of electrochemically inactive surfaces (the (001) surface).[38] We assume that the iSCAT images of the exposed surface of the particle (to a depth of ~330 nm, see Supplementary section 2) are representative of phenomena in the rest of the bulk, and can be compared to our simulations. Additionally, our simulations ignore any coupling of phenomena between adjacent layers in the structure. The electronic conductivity is also neglected, which means that the lithium mobility is considered to be smaller than the electron mobility (see *The effect of the electronic conductivity and composition on the calculations* below).

Supplementary Table 2: Values of constants used in phase field modelling.

Constant	Value used
C_{max}	51124.74 mol m^{-3}
T	300 K
a	5
b	76.2585
c	245.7523
d	305.4364
e	119.8260
C_{el}	1000 mol m^{-3}
α	0.5
k_0	2.6×10^{-11} $m^{5/2}$ $mol^{-1/2}$ s^{-1}
μ_0	-464551 J mol^{-1}
Ω_1	-159744 J mol^{-1}
Ω_2	-118782 J mol^{-1}
Ω_3	-39032 J mol^{-1}

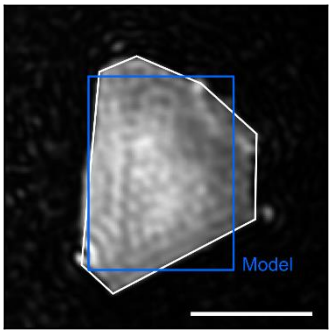

Supplementary Figure 4: Size of modelled LCO particle.
Raw iSCAT image of experimentally observed LCO particle with the edge contours highlighted in white. The blue rectangle is the edge contours of the *XY*-plane of the modelled system. The areas defined by the white contours and blue rectangle are equal (48 μm^2). Scale bar is 5 μm.

Choice of $g_h(x)$

The homogenous free energy can be found by integrating the homogenous lithium chemical potential in LCO, μ_h, which can be obtained from the open circuit voltage (E_{OC}) of a LCO half-cell according to

$$\mu_h = \partial g_h/\partial x = - E_{OC} F. \quad (9.9)$$

Note that for $0.77 < x < 0.95$, the measured E_{OC} correspond to a phase-separated (inhomogeneous) system. The energy of the corresponding homogenous system could be found by calculating the unstable solid solution pathway using density functional theory (DFT)[39], but such calculations have not been performed to the necessary level of detail for LCO. Instead, an approximation of the homogenous free energy can be obtained using the Redlich-Kister equation.[35] In this work, the chemical potential μ_h is expressed with equation 9.10 and the obtained voltage is shown in Supplementary Figure 5. Note that, using this approach, the

homogeneous free energy has no physical meaning for $0.77 < x < 0.95$, but it allows a phase separation to be simulated in that concentration range.[34]

$$\mu_{\mathrm{h}} = -x_{\max}\left[\begin{array}{l}\mu_0 + RT\left(\ln\left(x\right) - \ln\left(1-x\right)\right) + \left(1-2x\right)\left(\Omega_1 + \Omega_2\left(1-2x\right) + \Omega_3\left(1-2x\right)^2\right) \\ +x\left(1-x\right)\left(-2\Omega_2 - 4\Omega_3 - 8x\Omega_3\right)\end{array}\right] \quad (9.10)$$

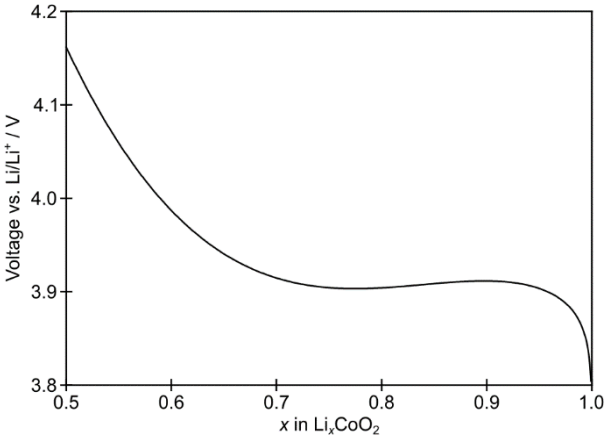

Supplementary Figure 5: **Voltage of the homogeneous phase**
Voltage of the homogenous phase as a function of lithium-content, obtained from the Redlich-Kister equation describing the chemical potential ($V = -\mu_{\mathrm{h}}/F$).

Choice of the pre-exponential factor of Butler-Volmer equation

In previous work, various types of pre-exponential factors have been used for the Bulter-Volmer equation: constants,[40] factors which depend on lithium concentration (as proposed by Newman *et al.*),[41–43] or factors which depend on the activity (as used by Bazant *et al.*)[35,44]. In this work, we compared concentration profiles calculated using both constant and concentration-dependent pre-exponential factors, for which the results lead to similar qualitative conclusions. For our choice of constant k_0 (Supplementary Table 2), the resulting exchange current density takes values from 0.01 – 0.1 mA cm^{-2}, which is in the same order of magnitude as typical values for insertion materials.[45]

The effect of the electronic conductivity and composition on the calculations

It is a good approximation to consider that the electron mobility is higher than the lithium mobility in the metallic phases (Li_xCoO_2 for $x < 0.77$). For the semiconducting phases (Li_xCoO_2 for $x > 0.95$), this has to be verified. We have used the Nernst-Einstein equation to estimate the conductivity σ (S m^{-1}) due to lithium-ions in Li_1CoO_2:

$$\sigma = D_{\mathrm{self}} \cdot Hr \cdot C \cdot \frac{q^2}{k_{\mathrm{B}}T}, \quad (9.11)$$

where D_{self} is the self-diffusion coefficient ($m^2\ s^{-1}$), Hr is the Haven ratio, C is the charge carrier concentration (m^{-3}), q is the carrier charge, and k_B is the Boltzmann constant ($J\ K^{-1}$). Using D_{self} = $10^{-16}\ m^2\ s^{-1}$ obtained from Van der Ven *et al.* and considering a Haven ratio of Hr = 1, σ is found to be on the order of magnitude of 10^{-5} S m^{-1}.[36,46] This value is much lower than the reported conductivities for Li_1CoO_2 (~10^{-1} S/m) suggesting that the electron mobility is significantly higher than the lithium mobility in lithium-rich Li_xCoO_2 ($x > 0.95$).[47]

The Redlich-Kister equation typically gives $Li_{0.95}CoO_2$ and $Li_{0.73}CoO_2$ for the limits of the solid solution regimes on either side of the insulator-metal biphasic transition; these values reflect compositions obtained for typical LCOs and are close to the electrochemistry shown here. We note that highly stoichiometric LCO samples, with a very low concentration of defects (not typical of commercial samples), have been shown to have a wider immiscibility gap, with the biphasic transition starting as early as the $Li_{0.99}CoO_2$ composition.[12] Future work will explore the effect of composition and (intentional) doping on the movement of phase fronts in greater detail.

(ii) The influence of κ and the absence of stress energy

To determine κ in a 1D model, Cahn *et al.* proposed[33]

$$\Delta f(C_{Li}) = \kappa \nabla x^2, \quad (9.12)$$

where $\Delta f(C_{Li})$ is the difference between the homogenous free energy and the free energy of a phase separated system. However, for LCO, this expression cannot be used, as the homogenous free energy is unknown. An alternative method, previously reported for $LiFePO_4$, calculates κ using the interfacial chemical energy, but this is also unknown for LCO.[48] Turning towards reported phase field models of LCO, values of κ/dy^2 (where dy is the mesh size used to calculate ∇x^2) vary widely from 0 to 10^5 J m^{-3}.[35,41,42,49] Given that $\mu_h(x)$ is of the order of 10^{10} J m^{-3}, these values of κ correspond to only a very small contribution of the energy penalty due to the concentration gradient.

To determine a suitable value of κ/dy^2 for our simulations of LCO, we explored the effect of varying κ/dy^2 from 0 to $6.25 \cdot 10^8$ J m^{-3} on the lithium concentration profile during lithiation and delithiation at 10C. All simulations with $\kappa/dy^2 \leq 6.25 \cdot 10^6$ J m^{-3} gave similar results and therefore lithium concentration profiles are plotted for $6.25 \cdot 10^6$ J $m^{-3} \leq \kappa/dy^2 \leq 6.25 \cdot 10^8$ J m^{-3} (Supplementary Figures 6 and 7).

For the delithiation (Supplementary Figure 6), we make three observations. Firstly, at x = 0.9, the lithium-poor phase forms relatively evenly around all active surfaces of the

simulated particle for lower κ/dy^2 values, while for higher values of κ/dy^2, the lithium-poor phase nucleates at distinct points. In other words, the interface between the lithium-rich and the lithium-poor phase appears to be reduced at higher κ/dy^2. Secondly, during further delithiation at $x = 0.8$, for values of $\kappa/dy^2 < 6.25 \cdot 10^8$ J m^{-3}, there is no lithium-rich phase (red) at the particle edges. Instead, the lithium-rich centre is entirely surrounded by the lithium-poor phase (blue). This behaviour corresponds to the 'shrinking core' mechanism. For $\kappa/dy^2 = 6.25 \cdot 10^8$ J m^{-3}, the lithium-rich phase is still present at the surface of the particle at $x = 0.8$, corresponding to an 'intercalation wave mechanism'. (Note that due to the symmetry of the rectangular cross-section in this system, the phase boundary advances equally from both short sides of the particle, while this would not have to be the case for more asymmetric particles). Thirdly, as the interfacial energy increases, intermediate Li_xCoO_2 phases with $0.95 < x < 0.77$ form at the phase boundary, making it more diffuse.

For the simulations during lithiation (Supplementary Figure 7), a reduced and more diffuse interface between the lithium-poor and lithium-rich phases is still observed at higher κ/dy^2 values. However, the shrinking core mechanism is observed for $\kappa/dy^2 \leq 6.25 \cdot 10^6$ J m^{-3}, which is two orders of magnitude lower than for the delithiation. Moreover, during the shrinking core mechanism at low κ/dy^2, the accumulation of the poorly conducting lithium-rich phase at the surface prevents further lithiation, increasing the overpotential and causing the reaction to shut down as the calculated voltage reaches the cut-off limit.

Our iSCAT experiments suggest that it is possible to lithiate the particle at nearly 10C via an intercalation wave mechanism, hence $\kappa/dy^2 = 1 \cdot 10^8$ J m^{-3} is chosen for the rest of the calculations presented. We strongly emphasize that this value is not a physical value because we have not taken the stress energy into account. Indeed, including the stress energy would also lead to a reduction of the interface between the lithium-rich/lithium-poor phases and therefore a switch between both mechanisms for the lithiation. Consequently, the width of the diffuse interfaces modelled in this work are overestimated.

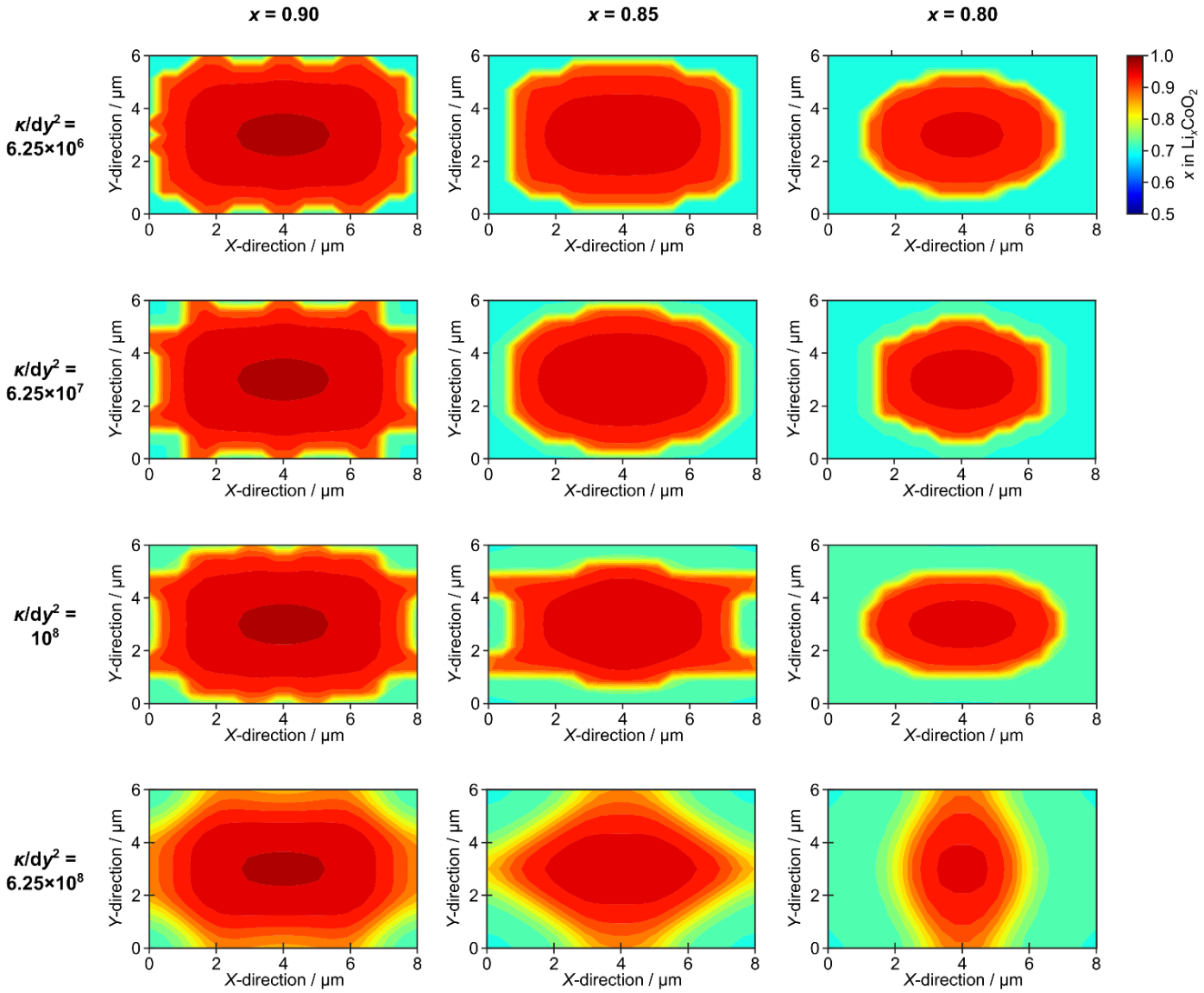

Supplementary Figure 6: Simulated lithium concentration profiles for the biphasic transition during delithiation at 10C with different κ/dy^2 (in J/m^3)

Simulated lithium concentrations (in *XY*-plane) during lithiation 10C with κ/dy^2 varying from $6.25 \cdot 10^6$ J m^{-3} (top) to $6.25 \cdot 10^8$ J m^{-3} (bottom). Three different overall states of charge are plotted: x = 0.9, 0.85, 0.8 for each κ/dy^2 value.

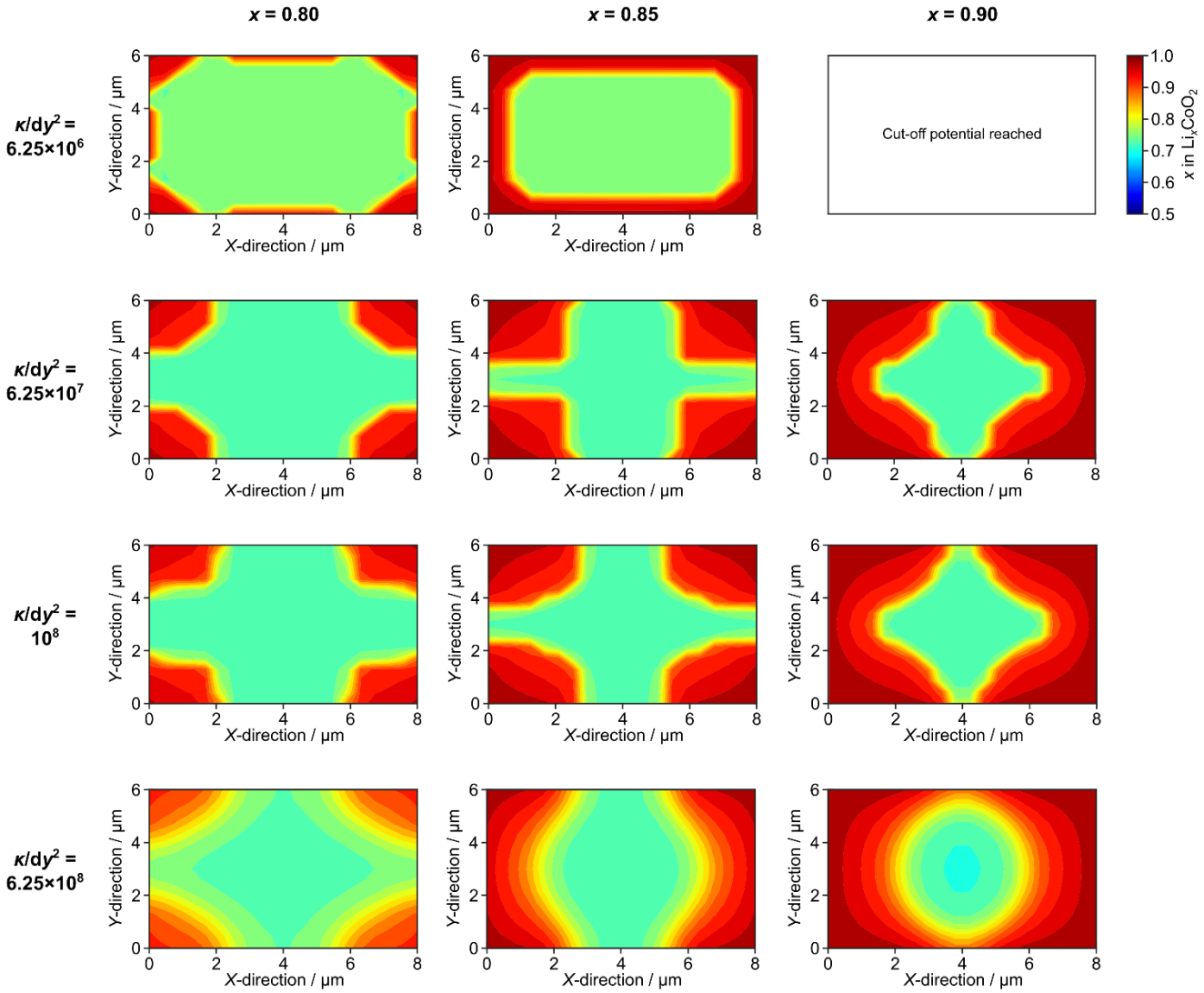

Supplementary Figure 7: Simulated lithium concentration profiles for the biphasic transition during lithiation at 10C with different κ/dy^2.

Simulated lithium concentrations (in *XY*-plane) during lithiation 10C with κ/dy^2 varying from $6.25 \cdot 10^6$ J m^{-3} (top) to $6.25 \cdot 10^8$ J m^{-3} (bottom). Three different overall states of charge are plotted: $x = 0.8$, 0.85, 0.9 for each κ/dy^2, apart from $\kappa/dy^2 = 6.25 \cdot 10^6$ J m^{-3}. In this case, the lithiation leads to the formation of the lithium-rich phase (red) over the entire active surface, causing the overpotential to reach the cut-off voltage (3 V). An intercalation wave mechanism is observed for higher values of κ/dy^2. Note that due to the symmetry of the rectangular cross-section in this simulated system, the phase boundary advances equally from both short sides of the particle during the intercalation wave mechanism, while this would not have to be the case for more asymmetric particles.

(iii) The influence of C-rate

The influence of the C-rate (2C or 10C) on the lithium concentration profile was simulated for delithiation (Supplementary Figure 8) and lithiation (Supplementary Figure 9). During delithiation, an intercalation wave mechanism is observed at 2C and a shrinking core mechanism is observed at 10C. The simulated shrinking core mechanism upon delithiation at 10C is consistent with our experimental observations (Figure 3). Additionally, the switch from a shrinking core to an intercalation wave mechanism upon reducing the C-rate is consistent with previous calculations,[50] and is supported by our experimental observations at the lower C-rates (Figure 4). For the lithiation, only the intercalation wave mechanism is observed, again consistent with our experimental observations.

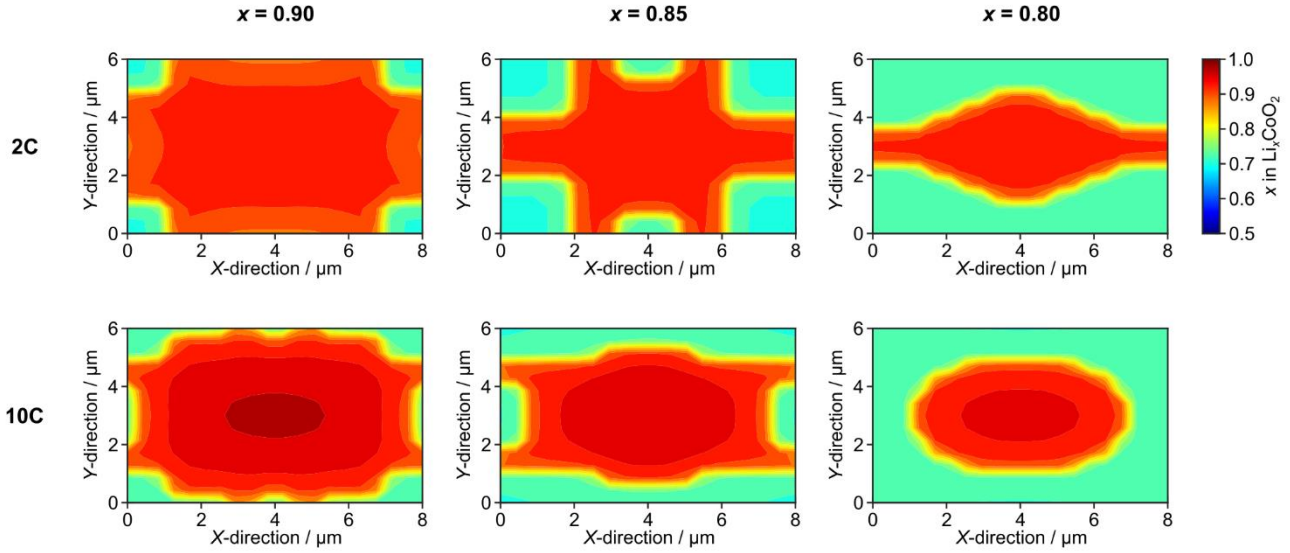

Supplementary Figure 8: Simulated lithium concentration profiles for the biphasic transition during delithiation at 2C and 10C.
Simulated lithium concentrations (in *XY*-plane) during delithiation at 2C (top) and at 10C (bottom). Three overall states of charge are plotted for each C-rate: x = 0.9, 0.85, 0.8.

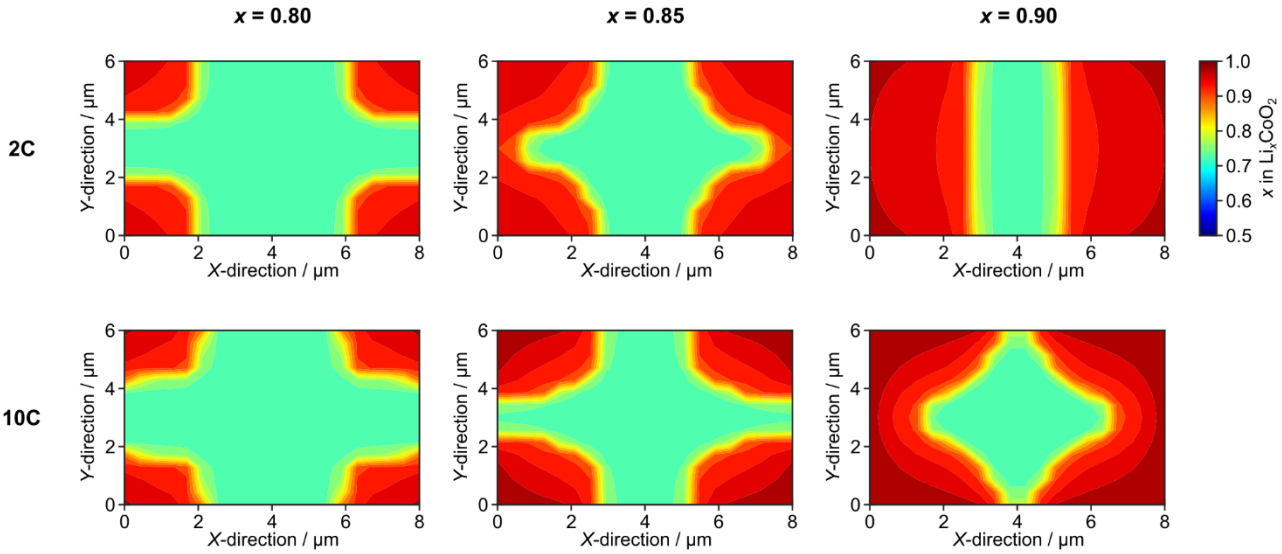

Supplementary Figure 9: Simulated lithium concentration profiles for the biphasic transition during lithiation at 2C and 10C.

Simulated lithium concentrations (in *XY*-plane) during lithiation at 2C (top) and at 10C (bottom). Three overall states of charge are plotted for each C-rate: x = 0.8, 0.85, 0.9. The phase boundary evolution (intercalation wave mechanism) is very similar between the two C-rates. A shrinking core mechanism for lithiation is only seen in our simulations at much higher C-rates (~30C).

(iv) Phase boundary speeds, determination of D_{self}

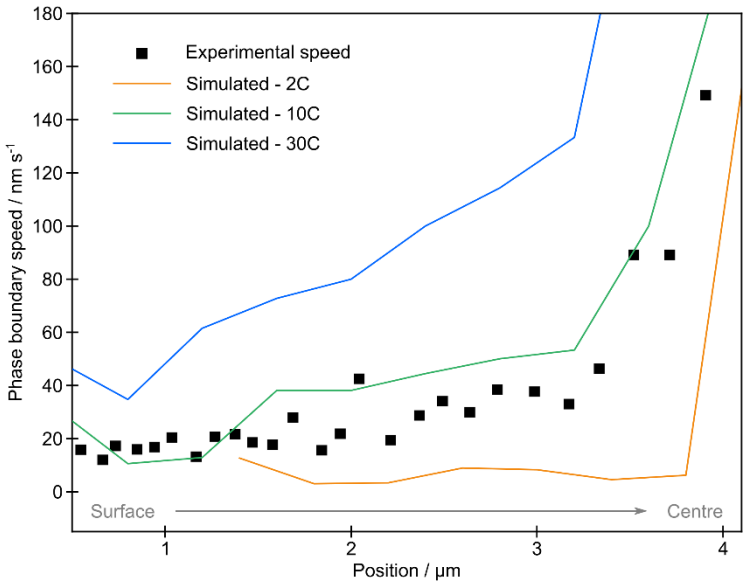

Supplementary Figure 10: Simulated speeds of the phase boundary during delithation at various C-rates.
The simulated phase boundary speeds were extracted (along the *X*-axis, at *Y* = 3 µm) for delithiation at 10C (green) and 30C (blue). At 2C (orange), the speed of the front was extracted along the Y-axis, perpendicular to the moving front. In all cases, the speed of the phase boundary increases as it approaches the centre of the particle. This can be explained by the decreasing surface area of the phase boundary – since the current is unchanged, the phase boundary speed must increase to maintain a fixed rate of conversion from lithium-rich to lithium-poor phase. Black squares indicate the experimentally observed phase boundary speed during delithiation (for the data presented in Figure 2), which was determined as described in Supplementary section 4. There is good agreement between the experimental speed and the simulated speed at 10C, which is consistent with the experimentally determined single-particle C-rate.

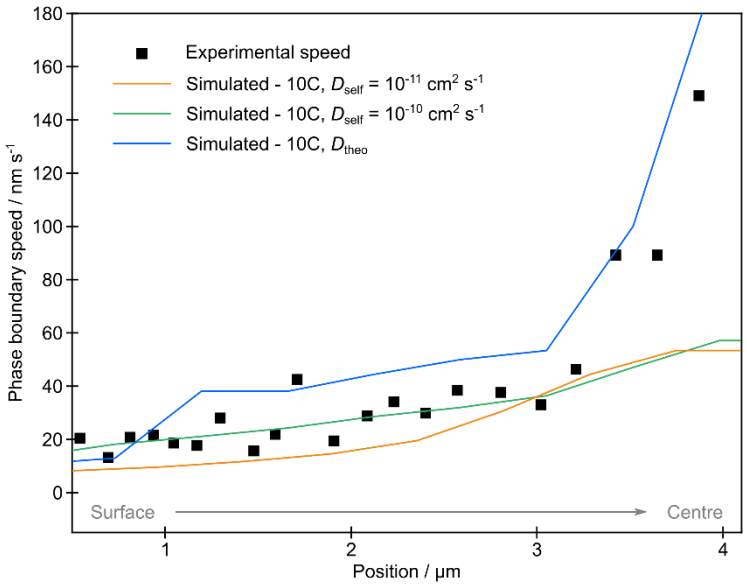

Supplementary Figure 11: Simulated speeds of the phase boundary during delithation at 10C, with various D_{self}.

The simulated phase boundary speeds were extracted (along the *X*-axis, at $Y = 3$ µm) for delithiation at 10C, using different values of the lithium self-diffusion coefficient, D_{self}. Phase boundary speeds plotted in blue were calculated using the diffusion coefficient reported by Van der Ven *et al.*[36] (referred to here as D_{theo} and used in all our simulations unless specified otherwise). Phase boundary speeds plotted in green and orange were calculated using lower constant diffusion coefficients of 10^{-10} cm^2 s^{-1} and 10^{-11} cm^2 s^{-1}, respectively. The phase boundary speeds simulated using 10^{-10} cm^2 s^{-1} and 10^{-11} cm^2 s^{-1} deviate significantly from the experimentally determined phase boundary speeds close to the centre of the particle (black squares). For the higher diffusion coefficients ($D_{theo} \approx 10^{-9}$ cm^2 s^{-1} for $x \approx 0.75$), there is good agreement with the experiment, suggesting that $D_{self} > 10^{-10}$ cm^2 s^{-1} for $x \approx 0.75$. The corresponding lower bound value of the chemical diffusion coefficient (calculated using the thermodynamic factor[51]) is shown in Supplementary Figure 13, along with previously reported values.

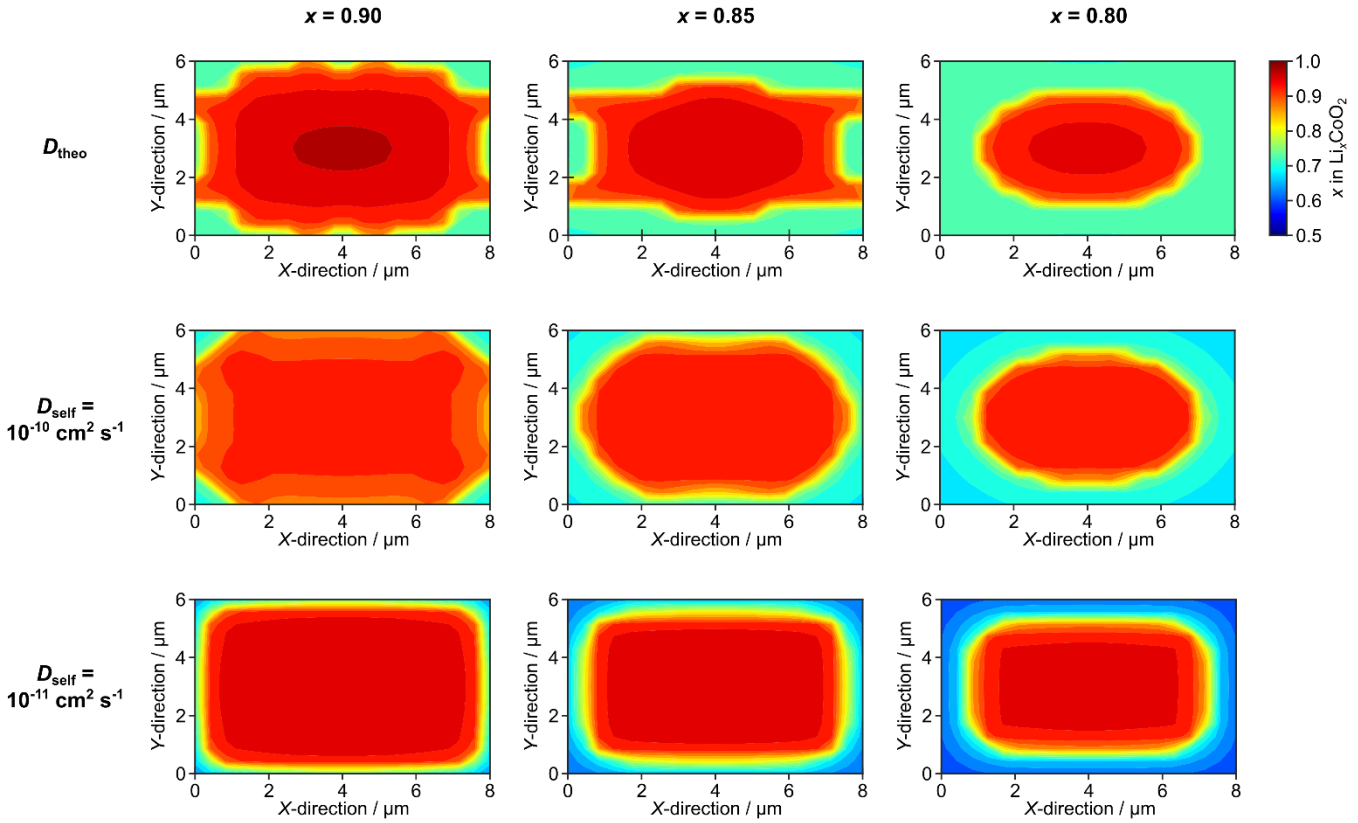

Supplementary Figure 12: Simulated lithium concentration profiles during delithation at 10C, with various D_{self}.

Simulated Li concentrations (in *XY*-plane) during delithiation at 10C, for overall states of charge of x = 0.9, 0.85, and 0.8. As referred to in Supplementary Figure 11, three different self-diffusion coefficients are used. The top set of panels corresponds to the higher values reported by Van der Ven *et al.*[36] (referred to here as D_{theo}), the middle set corresponds to a constant value of D_{self} =10^{-10} cm^2 s^{-1}, and the bottom set of 10^{-11} cm^2 s^{-1}. In the middle and bottom set, severe concentration gradients develop in the lithium-poor phase (blue), with the concentration at the surface of the particle reaching nearly $Li_{0.5}CoO_2$ for the bottom set. Upon further delithiation, the low lithium concentration at the surface means that the voltage reaches the cut-off value of 4.2 V before the biphasic transition is completed. This is not the case for the higher diffusion coefficients (top), where the biphasic transition is completed within the set voltage range, as is observed experimentally. These concentration profiles help us to understand why the phase boundary speeds for D_{self} = 10^{-11} cm^2 s^{-1} deviate from the experimental values (Supplementary Figure 11). In this case, the lithium ions cannot diffuse through the lithium-poor phase quickly enough to achieve the phase boundary propagation speed necessarily for a purely biphasic process, instead leading to a pronounced concentration gradient at the particle surface and lower phase boundary speeds.

(v) Comparison of previously reported diffusion coefficients for LCO

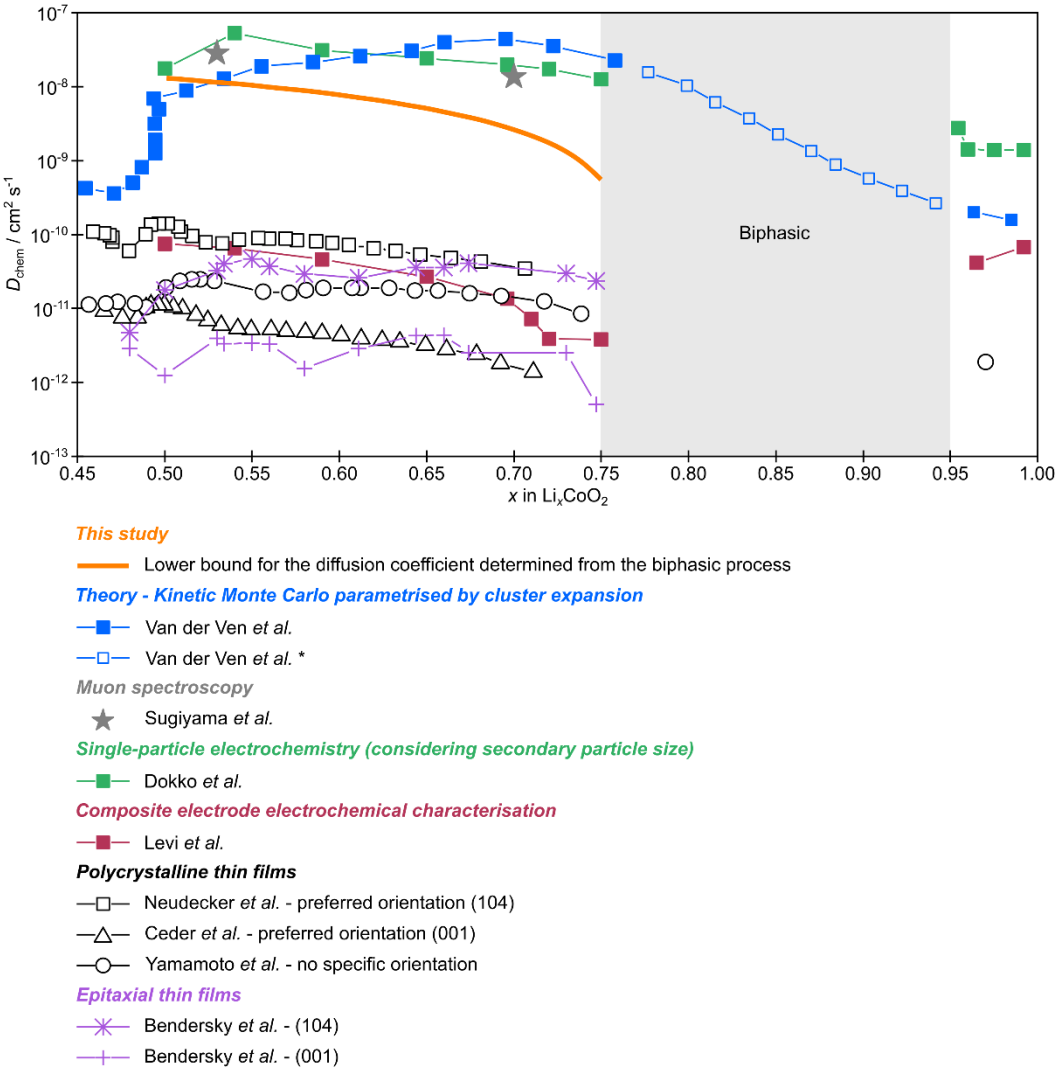

Supplementary Figure 13: Comparison of reported values for the chemical diffusion coefficient in LCO, including values obtained in this work.
Previously, high diffusion coefficient values have been reported based on simulations[36] and muon spectroscopy[52], while lower values of ~10^{-11} cm^2 s^{-1} have been obtained by electrochemical methods (such as PITT or GITT) on polycrystalline and epitaxial thin films or composite electrode films[38,53–55]. Additionally, Dokko *et al.* performed PITT experiments on a single LCO secondary particle and reported a high diffusion coefficient, with the characteristic distance for diffusion being the size of the secondary particle.[56] In our work, we have determined a lower bound for the chemical diffusion coefficient of ~10^{-9} cm^2 s^{-1}, as detailed in Supplementary Figure 11. This value is in agreement with the previous results from muon spectroscopy[52] and theoretical calculations[36]. Note that our lower bound for the chemical diffusion coefficient was determined at the limit of the biphasic transition, and extrapolated to x = 0.5 by considering a constant self-diffusion coefficient. We highlight in grey the miscibility gap for the biphasic transition, using the typically quoted limiting compositions. Within the miscibility gap (for $0.75 < x < 0.95$), values for the chemical diffusion coefficient are not physical, since phase separation occurs. (*The theoretical work shown with hollow blue squares assumes a hypothetical homogenous system in this region).

10. References

1. Mahmoodabadi, R. G. *et al.* Point spread function in interferometric scattering microscopy (iSCAT). Part I: aberrations in defocusing and axial localization. *Opt. Express* **28**, 25969–25988 (2020).
2. Mojarad, N., Sandoghdar, V. & Krishnan, M. Measuring three-dimensional interaction potentials using optical interference. *Opt. Express*, **21**, 9377–9389 (2013).
3. Ortega-Arroyo, J. & Kukura, P. Interferometric scattering microscopy (iSCAT): new frontiers in ultrafast and ultrasensitive optical microscopy. *Phys. Chem. Chem. Phys.* **14**, 15625–15636 (2012).
4. Piliarik, M. & Sandoghdar, V. Direct optical sensing of single unlabelled proteins and super-resolution imaging of their binding sites. *Nat. Commun.* **5**, 4495 (2014).
5. Ménétrier, M., Saadoune, I., Levasseur, S. & Delmas, C. The insulator-metal transition upon lithium deintercalation from $LiCoO_2$: electronic properties and ^7Li NMR study. *J. Mater. Chem.* **9**, 1135–1140 (1999).
6. Liu, H. L. *et al.* Electronic structure and lattice dynamics of Li_xCoO_2 single crystals. *New J. Phys.* **17**, 103004 (2015).
7. Akselrod, G. M. *et al.* Visualization of exciton transport in ordered and disordered molecular solids. *Nat. Commun.* **5**, 3646 (2014).
8. Sung, J. *et al.* Long-range ballistic propagation of carriers in methylammonium lead iodide perovskite thin films. *Nat. Phys.* **16**, 171–176 (2020).
9. Schnedermann, C. *et al.* Ultrafast tracking of exciton and charge carrier transport in optoelectronic materials on the nanometer scale. *J. Phys. Chem. Lett.* **10**, 6727–6733 (2019).
10. Delor, M., Weaver, H. L., Yu, Q. & Ginsberg, N. S. Imaging material functionality through three-dimensional nanoscale tracking of energy flow. *Nat. Mater.* **19**, 56–62 (2020).
11. Reimers, J. N. & Dahn, J. R. Electrochemical and in situ X-ray diffraction studies of lithium intercalation in Li_xCoO_2. *J. Electrochem. Soc.* **139**, 2091–2097 (1992).

12. Ménétrier, M., Carlier, D., Blangero, M. & Delmas, C. On "really" stoichiometric $LiCoO_2$. *Electrochem. Solid-State Lett.* **11**, A179 (2008).

13. Griffith, K. J., Wiaderek, K. M., Cibin, G., Marbella, L. E. & Grey, C. P. Niobium tungsten oxides for high-rate lithium-ion energy storage. *Nature* **559**, 556–563 (2018).

14. Koçer, C. P., Griffith, K. J., Grey, C. P. & Morris, A. J. Cation disorder and lithium insertion mechanism of Wadsley–Roth crystallographic shear phases from first principles. *J. Am. Chem. Soc.* **141**, 15121–15134 (2019).

15. Yang, Y. *et al.* Achieving ultrahigh-rate and high-safety Li^+ storage based on interconnected tunnel structure in micro-size niobium tungsten oxides. *Adv. Mater.* **32**, 1905295 (2020).

16. Liu, Y., Zhu, Y. & Cui, Y. Challenges and opportunities towards fast-charging battery materials. *Nat. Energy* **4**, 540–550 (2019).

17. Otoyama, M., Kowada, H., Sakuda, A., Tatsumisago, M. & Hayashi, A. Operando confocal microscopy for dynamic changes of Li^+ ion conduction path in graphite electrode layers of all-solid-state batteries. *J. Phys. Chem. Lett.* **11**, 900–904 (2020).

18. Kazyak, E. *et al.* Li penetration in ceramic solid electrolytes: operando microscopy analysis of morphology, propagation, and reversibility. *Matter* **2**, 1025–1048 (2020).

19. Wood, K. N. *et al.* Dendrites and pits: untangling the complex behavior of lithium metal anodes through operando video microscopy. *ACS Cent. Sci.* **2**, 790–801 (2016).

20. Namink, K., Meng, X., Koper, M. T. M., Kukura, P. & Faez, S. Electric-double-layer-modulation microscopy. *Phys. Rev. Applied* **13**, 044065 (2020).

21. Liu, D. *et al.* Review of recent development of in situ/operando characterization techniques for lithium battery research. *Adv. Mater.* **31**, 1806620 (2019).

22. Deng, Z. *et al.* Recent progress on advanced imaging techniques for lithium-ion batteries. *Adv. Energy Mater.* **11**, 2000806 (2021).

23. Wang, Y. High-resolution 3D imaging and material analysis with transmission X-ray microscopy and nano-CT. In *Characterization of Materials*. John Wiley and Sons (2012).

24. Bak, S.-M., Shadike, Z., Lin, R., Yu, X. & Yang, X.-Q. In situ/operando synchrotron-based X-ray techniques for lithium-ion battery research. *NPG Asia Mater.* **10**, 563–580 (2018).

25. Wu, Y. & Liu, N. Visualizing battery reactions and processes by using in situ and in operando microscopies. *Chem* **4**, 438–465 (2018).

26. Chen, C.-Y. *et al.* Visualization of Si anode reactions in coin-type cells via operando scanning electron microscopy. *ACS Appl. Mater. Interfaces* **9**, 35511–35515 (2017).

27. Chen, D., Indris, S., Schulz, M., Gamer, B. & Mönig, R. In situ scanning electron microscopy on lithium-ion battery electrodes using an ionic liquid. *J. Power Sources* **196**, 6382–6387 (2011).

28. Wu, F. & Yao, N. Advances in sealed liquid cells for in-situ TEM electrochemial investigation of lithium-ion battery. *Nano Energy* **11**, 196–210 (2015).

29. Singh, G. K., Ceder, G. & Bazant, M. Z. Intercalation dynamics in rechargeable battery materials: general theory and phase-transformation waves in $LiFePO_4$. *Electrochim. Acta* **53**, 7599–7613 (2008).

30. Cogswell, D. A. & Bazant, M. Z. Size-dependent phase morphologies in $LiFePO_4$ battery particles. *Electrochem. commun.* **95**, 33–37 (2018).

31. de Klerk, N. J. J., Vasileiadis, A., Smith, R. B., Bazant, M. Z. & Wagemaker, M. Explaining key properties of lithiation in TiO_2-anatase Li-ion battery electrodes using phase-field modeling. *Phys. Rev. Materials* **1**, 025404 (2017).

32. Han, B. C., Van der Ven, A., Morgan, D. & Ceder, G. Electrochemical modeling of intercalation processes with phase field models. *Electrochim. Acta* **49**, 4691–4699 (2004).

33. Cahn, J. W. & Hilliard, J. E. Free energy of a nonuniform system. I. interfacial free energy. *J. Chem. Phys.* **28**, 258–267 (1958).

34. Redlich, O. & Kister, A. T. Algebraic representation of thermodynamic properties and the classification of solutions. *Ind. Eng. Chem.* **40**, 345–348 (1948).

35. Nadkarni, N., Zhou, T., Fraggedakis, D., Gao, T. & Bazant, M. Z. Modeling the metal–insulator phase transition in Li_xCoO_2 for energy and information storage. *Adv. Funct. Mater.* **29**, 1902821 (2019).

36. Van der Ven, A. & Ceder, G. Lithium diffusion in layered Li_xCoO_2. *Electrochem. Solid-State Lett.* **3**, 301 (2000).

37. Doyle, M., Fuller, T. F. & Newman, J. Modeling of galvanostatic charge and discharge of the lithium/polymer/insertion cell. *J. Electrochem. Soc.* **140**, 1526 (1993).

38. Takeuchi, S. *et al.* Epitaxial $LiCoO_2$ films as a model system for fundamental electrochemical studies of positive electrodes. *ACS Appl. Mater. Interfaces* **7**, 7901–7911 (2015).

39. Malik, R., Zhou, F. & Ceder, G. Kinetics of non-equilibrium lithium incorporation in $LiFePO_4$. *Nat. Mater.* **10**, 587–590 (2011).

40. Mendoza, H., Roberts, S. A., Brunini, V. E. & Grillet, A. M. Mechanical and electrochemical response of a $LiCoO_2$ cathode using reconstructed microstructures. *Electrochim. Acta* **190**, 1–15 (2016).

41. Yamakawa, S., Nagasako, N., Yamasaki, H., Koyama, T. & Asahi, R. Phase-field modeling of stress generation in polycrystalline $LiCoO_2$. *Solid State Ion.* **319**, 209–217 (2018).

42. Malavé, V., Berger, J. R., Zhu, H. & Kee, R. J. A computational model of the mechanical behavior within reconstructed Li_xCoO_2 Li-ion battery cathode particles. *Electrochim. Acta* **130**, 707–717 (2014).

43. Fuller, T. F., Doyle, M. & Newman, J. Simulation and optimization of the dual lithium ion insertion cell. *J. Electrochem. Soc.* **141**, 1 (1994).

44. Bazant, M. Z. Theory of chemical kinetics and charge transfer based on nonequilibrium thermodynamics. *Acc. Chem. Res.* **46**, 1144–1160 (2013).

45. Tsai, P.-C. *et al.* Single-particle measurements of electrochemical kinetics in NMC and NCA cathodes for Li-ion batteries. *Energy Environ. Sci.* **11**, 860–871 (2018).

46. Murch, G. E. The haven ratio in fast ionic conductors. *Solid State Ion.* **7**, 177–198 (1982).

47. Tukamoto, H. & West, A. R. Electronic conductivity of $LiCoO_2$ and its enhancement by magnesium doping. *J. Electrochem. Soc.* **144**, 3164–3168 (1997).

48. Abdellahi, A., Akyildiz, O., Malik, R., Thornton, K. & Ceder, G. The thermodynamic stability of intermediate solid solutions in $LiFePO_4$ nanoparticles. *J. Mater. Chem. A* **4**, 5436–5447 (2016).

49. Yamakawa, S., Yamasaki, H., Koyama, T. & Asahi, R. Numerical study of Li diffusion in polycrystalline $LiCoO_2$. *Journal of Power Sources* **223**, 199–205 (2013).

50. Fraggedakis, D. *et al.* A scaling law to determine phase morphologies during ion intercalation. *Energy Environ. Sci.* **13**, 2142–2152 (2020).

51. Van der Ven, A., Bhattacharya, J. & Belak, A. A. Understanding Li diffusion in Li-intercalation compounds. *Acc. Chem. Res.* **46**, 1216–1225 (2013).

52. Sugiyama, J. *et al.* Li diffusion in Li_xCoO_2 probed by muon-spin spectroscopy. *Phys. Rev. Lett.* **103**, 147601 (2009).

53. Jang, Y.-I., Neudecker, B. J. & Dudney, N. J. Lithium diffusion in Li_xCoO_2 ($0.45 < x < 0.7$) intercalation cathodes. *Electrochem. Solid-State Lett.* **4**, A74 (2001).

54. Xia, H., Lu, L. & Ceder, G. Li diffusion in $LiCoO_2$ thin films prepared by pulsed laser deposition. *J. Power Sources* **159**, 1422–1427 (2006).

55. Xie, J. *et al.* Orientation dependence of Li–ion diffusion kinetics in $LiCoO_2$ thin films prepared by RF magnetron sputtering. *Solid State Ionics* **179**, 362–370 (2008).

56. Dokko, K. *et al.* Kinetic characterization of single particles of $LiCoO_2$ by AC impedance and potential step methods. *J. Electrochem. Soc.* **148**, A422 (2001).